Master's thesis

NTNU
Norwegian University of Science and Technology
Faculty of Natural Sciences
Department of Physics

Elisabeth Bruun Karud

Reconstructing surface morphology using coherent X-ray diffraction combined with iterative phase retrieval algorithms

Master's thesis in Applied Physics and Mathematics
Supervisor: Dag Werner Breiby
June 2019

NTNU
Kunnskap for en bedre verden

Elisabeth Bruun Karud

Reconstructing surface morphology using coherent X-ray diffraction combined with iterative phase retrieval algorithms

Master's thesis in Applied Physics and Mathematics
Supervisor: Dag Werner Breiby
June 2019

Norwegian University of Science and Technology
Faculty of Natural Sciences
Department of Physics

NTNU
Norwegian University of
Science and Technology

Abstract

Inversion of scattering data is a comprehensive problem in X-ray physics and generally amounts to the phase problem. In scattering experiments only the intensity is measured, whereas the phase information is lost. A direct inversion of the scattering data to reconstruct the scattering object is not possible without the phase information. In many applications, such as in grazing incidence small-angle X-ray scattering and X-ray reflectivity, a model is fitted with experimental parameters and used to provide information of the scattered object. The models are often built on an assumption of an incoming plane wave, after which a correction to account for the beam divergence must be applied. By substituting the plane wave with a more realistic model for the experimental beam, such as the Gaussian beam, the modelling techniques may be improved. Correcting for the beam divergence will no longer be necessary as the beam divergence is an inherent parameter of the Gaussian beam.

The first part of this thesis investigates the propagation and reflection of the Gaussian beam using the angular decomposition method. Mathematically the Gaussian beam can be derived from the Helmholtz equation and is found to be in good agreement with the Gaussian beam from the angular decomposition method. Reflecting surfaces such as multilayered structures and scattering from nanostructures in grazing incidence have been investigated with the Gaussian beam. In both cases the reflectivity of the Gaussian beam in the limit of a huge beam waist was found to be in good agreement with the reflectivity of a plane wave. It was also found that with decreasing beam waist the Gaussian beam lack important features in the reflectivity, and is therefore not suitable in reflectivity experiments.

The second half of the project was dedicated to coherent X-ray imaging. Given oversampling in Fourier space, iterative algorithms can retrieve the lost phase information. The study was limited to coherent X-ray diffraction on rough surfaces in grazing incidence. In addition, the surface was considered to be one-dimensional as the footprint in grazing incidence is very elongated and the illuminating beam very narrow. The goal was to reconstruct the phase information, and in doing so reconstruct the surface morphology. Three iterative numerical algorithms have been compared; the Gerchberg-Saxton algorithm, the Hybrid input-output algorithm and a combination of these two. The two former are shown to stagnate resulting in an unsatisfactory solution. However, the combination of the two produces small reconstruction errors. The reconstructed surface morphology improves rapidly using the Hybrid input-output algorithm while the error decreases only slightly. Applying a few iterations of the Gerchberg-Saxton algorithm following a number of iterations with Hybrid input-output algorithm is shown to rapidly decrease the error and converge towards a satisfactory solution. An attempt was made to reconstruct the surface morphology of a hemispherical island on a surface using the combination algorithm. The qualitative shape of the reconstructions was found to be in good agreement with the shape of the island. However, the width and height of the island was reconstructed unsuccessfully.

Sammendrag

Inversjon av spredningsdata er et omfattende problem i røntgenfysikk og gir opphav til faseproblemet. I spredningseksperimenter blir bare intensiteten målt, mens faseinformasjonen er tapt. Rekonstruering av spredningsobjektet ved direkte invertering av spredningsdata er ikke mulig uten faseinformasjonen. I bruksområder som småvinkel-spredning (GISAXS) og spekulær refleksjon (XRR) blir modeller brukt for å få informasjon om spredningsobjektet. Modellene bygger på en antakelse om innkommende planbølger, og korrigering av bølgens spredning er derfor nødvendig. Erstattes planbølgen med en mer realistisk modell, som den Gaussiske bølgen, kan modelleringsteknikkene forbedres. Divergensen er en iboende egenskap ved den Gaussiske bølgen, og korrigering er derfor ikke nødvendig.

Denne masteroppgaven begynner med å undersøke propagasjon og refleksjon av Gaussiske bølger ved å dekomponere bølgen i planbølgekomponenter. Den Gaussiske bølgen kan matematisk utledes fra Helmholtz' likning, og den matematiske modellen stemmer godt overens med den Gaussiske bølgen dekomponert fra planbølgekomponentene. Oppgaven er avgrenset til å studere refleksjon av Gaussiske bølger på lagvise strukturer og Gaussiske bølger med liten innfallsvinkel på overflater med små partikler. Det ble i begge tilfeller vist at den reflekterte intensiteten til Gaussiske bølger med stor bredde samsvarer med den reflekterte intensiteten til planbølger. Den reflekterte intensiteten til Gaussiske bølger med mindre bredde manglet noen av de karakteristiske trekkene for reflektert intensitet, og er derfor ikke passende for slike eksperimenter.

Den andre delen av masteroppgaven undersøkte koherent røntgenavbildning (CXDI) begrenset til ujevne overflater og innkommende bølger med små innkommende vinkler. Fotavtrykket til bølgen blir avlangt når innkommende vinkel er liten, så overflaten kan derfor antas å være endimensjonal. Gitt at diffraksjonsmønsteret er samplet med samplingsrate lik halvparten av Nyquistfrekvensen, kan iterative algoritmer rekonstruere faseinformasjonen som også gir informajson om overflaten. Tre iterative algoritmer ble sammenlignet; Gerchberg-Saxton, Hybrid input-output og en kombinasjon av disse to. De to førstnevnte stagnerte før en tilfredsstillende løsning ble nådd. Formen til den rekonstruerte overflaten ble betydelig forbedret ved bruk av Hybrid input-output algoritmen selv om feilen bare avtok noe. Dersom noen få iterasjoner med Gerchberg-Saxton algoritmen etterfulgte et større antall iterasjoner med Hybrid input-output algoritmen, ble rekonstruksjonsfeilen betydelig mindre. Overflaten til en partikkel på et substrat ble forsøkt rekonstruert med kombinasjonsalgoritmen. Den kvalitative formen var i god overenstemmelse med formen til partikkelen, i motsetning til høyden og størrelsen til partikkelen.

Preface

This master thesis is succeeding my project thesis work from last fall. The project was limited to the study of fully coherent incoming Gaussian beam on a flat, non-absorbing material. The Gaussian beam was studied using the angular decomposition method. Some of the theory sections are partly based on the theory section from the project work. These sections include the section on electromagnetic waves (2.1), the Fresnel equations (2.2), GISAXS (2.5), coherence (2.6) and the mathematical description of the Gaussian beam (3.1). The project will be referred to as previous project work and cited as [1].

Acknowledgements

First and foremost, I would like to thank my supervisor Dag Werner Breiby for giving me the opportunity to study this topic and for thorough feedback throughout the year.

I would also want to thank Alain Gibaud for dicussions and encouragements during the last few weeks of this thesis.

Lastly, I would like to thank Tord Kriznik Sørensen for invaluable support during both ups and downs. When I needed new input and better point of view, he provided constructive feedback and new perspective.

Contents

Abstract i

Sammendrag iii

Preface v

Acknowledgements vii

Table of Contents x

1 Introduction 1

2 Theory of electromagnetism and optics 5
2.1 Electromagnetic waves 5
2.2 Fresnel equations 6
2.2.1 X-ray regime 8
2.3 Reflection from a film on a surface 8
2.4 Coordinate system 9
2.5 GISAXS 10
2.6 Coherence 14

3 The Gaussian beam 15
3.1 Mathematical description of the Gaussian beam 15
3.2 Analytical model for reflection of a gaussian beam 17

4 Phase reconstruction 21
4.1 Coherent X-ray diffraction 21
4.2 Coherent X-ray diffraction on a rough surface 22
4.3 Reconstruction of surface morphology from 1D speckle pattern 23
4.4 Gerchberg-Saxton algorithm 25
4.5 Other algorithms for the two intensity measurement problem 26

5 Results **29**
5.1 The Gaussian beam 29
5.2 Reflection of a Gaussian beam by a thin film 30
5.3 Scattering of a Gaussian beam on nanoscale islands in the GISAXS geometry 32
5.4 Reconstruction of 1D surface morphology by coherent GISAXS 34
5.5 Comparison with other reconstruction algorithms 38
5.6 Reconstructing the surface morphology in GISAXS geometry 41

6 Conclusion and outlooks **45**

Bibliography **47**

Chapter 1

Introduction

Wilhelm Conrad Rontgen discovered X-rays in 1895. Since then, X-rays have become an established and invaluable probe when studying the structure of matter. X-ray imaging utilizes the interaction of X-rays with matter through absorption and scattering. X-ray absorption is a useful tool for characterizing materials as the absorption process depends on the atomic number. The X-ray scattering process is widely used for studying atomic and molecular structures. In the 1970s synchrotron radiation was discovered as a more intense source for X-rays, which greatly increased the rate of innovation in X-ray science [2].

In scattering experiments the general problem is to construct an image of the scattered object from the scattering data. This is known as an inversion problem. From the diffraction pattern only the intensity can be measured whereas the phase information is lost. Without the phase information, a direct reconstruction of the scattered object is impossible. Fitting a model with experimental parameters can be used to indirectly provide information on the scattered object. This is for example done in grazing incidence small-angle X-ray scattering (GISAXS) and X-ray reflectivity (XRR) [3; 4].

GISAXS is a scattering technique used for probing nanoscale density inhomogeneities. The development of GISAXS is closely related to studying thin-film growth. The clusters, or islands, that formed on the thin-film surface were reduced to immeasurable quantities when using the predecessor of GISAXS, the small-angle X-ray scattering (SAXS) [5; 6]. SAXS is a technique for studying structures of colloidal size and can be used for characterization of polymers, metals, alloys, glasses and colloidal powders [7]. When using SAXS to study islands on surfaces, it is primarily done in transmission mode where the X-ray beam is directly pointed at the sample. Because of the small number of scattering objects in the beam path, the resulting signal-to-noise ratio is low [5]. By aligning the sample in a grazing incidence geometry the refracted evanescent wave will be confined to the top layer and increase the signal-to-noise ratio [5]. Ref. [6] later showed that GISAXS showed more potential using a synchrotron source in addition to a 2D detector. Compared to other techniques GISAXS is a non-invasive technique, can be used *in situ* and provides good sampling statistics [8]. GISAXS is therefore used in a range of research systems, amongst

them are islands on surfaces, discontinuous semiconductor superlattices and several soft condensed matter topics [8]. When studying islands on a surface it is possible to reveal size, shape and inner crystalline structure [9]. During these experiments the resulting diffraction pattern is only a measure of the beam intensity, whereas the phase information is lost. Several software packages exist making it possible to analyse the diffraction data and reconstruct the structure by modelling and fitting [3][4].

XRR is a technique for studying surfaces and multilayers. Ref. [10] was one of the first to investigate the reflected intensity as a function of incident angle. It was shown that formulas from the Fresnel formalism of reflection and refraction of multilayered structures can be used to analyse experimental reflectivity curves [11]. XRR has become a powerful method for studying the structure and organization of materials grown as thin films [12]. It is also useful to analyze roughness at multilayered interfaces [13] and liquid surfaces [14]. Since only the intensity is measured, it is necessary to compare the measured reflectivity to a reflectivity calculated from a model. Necessary factors to take into account when creating the model are geometrical and resolution-function factors [14]. These factors are especially important when considering small incident angles.

When fitting models to experimental data the incoming beam is assumed to be a plane wave. This enforces a correction to account for the divergence of the beam [14]. The correction is usually done by convoluting the calculated intensity for the ideal case with a Gaussian function. By substituting the plane wave assumption in favour of a more experimentally realistic beam, the Gaussian beam, the data models may be improved. This thesis will study the Gaussian beam using the angular decomposition method [15; 16]. Previous project work has investigated the amplitude of the reflected Gaussian beam [1]. In this thesis the propagation of the Gaussian beam will be investigated as well as how the wavefronts behave. Reflection of Gaussian beams at complex surfaces such as multilayered structures and islands on surfaces in the GISAXS geometry will also be considered. In addition, coherent imaging will be studied, which enables the phase to be reconstructed using numerical algorithms.

In coherent X-ray diffraction imaging (CXDI) the diffraction pattern is measured and then directly inverted to acquire a high-resolution image [17; 18]. Since the first experimental demonstration in 1999, coherent diffraction imaging has been applied to a wide range of scientific fields. Coherent diffraction can be classified into four categories [17]. The first is called plane-wave CDI where a plane wave is illuminating a finite object and a measurement of the far-field diffraction pattern is done. It can be implemented with high brilliance X-ray sources and has resulted in high spatial resolution [19]. The requirement of isolated objects is the main drawback. The second method is called scanning or ptychographic CDI. A circular aperture is used to define the illumination probe which is utilized to scan the sample, making a sequence of partially overlapping diffraction patterns. Compared to plane-wave CDI it can be applied to extended objects, however, for 3D images each projection requires a 2D scan that can cause the sample to vibrate and degrade the resolution. The third method is called Bragg CDI. It is mainly used for studying structures of nanocrystals as the intensity distribution at the Bragg reflections are related to the strain in the nanocrystal. The main advantages over the previous methods are that it yields information regarding ion displacements and the strain tensor inside the nanocrystal. Lastly, the fourth method is called Fresnel CDI where focusing optics is used to create a curved

wavefront which is used to illuminate the sample. Due to the curvature of the incident wave, the numerical image reconstruction is rapidly converging. On the other hand, it requires a very stable surface [17].

Given that the diffraction pattern from a CXDI experiment can be oversampled, it is possible to retrieve the phase information using iterative algorithms. Iterative algorithms using the Fourier modulus were developed in 1978 [20] and developed further through the 1980s and 1990s [21; 22]. One of the earlier algorithms was created by Gerchberg and Saxton [23] and was one of the first efficient solutions to the phase problem [24]. In this thesis the Gerchberg-Saxton algorithm will be studied and compared with other algorithms such as the Hybrid input-output algorithm [21] as tools for reconstructing a surface morphology.

This thesis begins by presenting an introduction to electromagnetic theory and optics in chapter two. In the third chapter the Gaussian beam is derived and a derivation for an analytical expression of the optical field near a reflective surface is provided. Chapter four investigates how CXDI can reconstruct the lost phase information from a diffraction pattern using numerical algorithms. Next, the fifth chapter presents and discusses the findings of this thesis. Chapter five begins by exploring the propagation of the Gaussian beam. Subsequently, the reflection of a beam on multilayered structures and reflection in the GISAXS geometry will be considered. Lastly, reconstruction of the phase information will be discussed using the methods and algorithms presented in chapter four. The last and sixth chapter will present the conclusions from this thesis.

Chapter 2

Theory of electromagnetism and optics

2.1 Electromagnetic waves

Electromagnetic waves propagate according to Maxwell's equations [25],

$$\nabla \cdot \boldsymbol{D} = \rho_f, \tag{2.1}$$

$$\nabla \times \boldsymbol{E} = -\frac{\partial \boldsymbol{B}}{\partial t}, \tag{2.2}$$

$$\nabla \cdot \boldsymbol{B} = \boldsymbol{0}, \tag{2.3}$$

$$\nabla \times \boldsymbol{H} = \boldsymbol{j_f} + \frac{\partial \boldsymbol{D}}{\partial t}, \tag{2.4}$$

with the constitutive relations $\boldsymbol{D} = \epsilon_0 \epsilon_r \boldsymbol{E}$ and $\boldsymbol{B} = \mu \boldsymbol{H}$. $\boldsymbol{D}$ is the electric displacement, ϵ_r is the dielectric constant, ϵ_0 is the permittivity of vacuum and μ is the permeability of the material. Maxwell's equations make up a set of coupled, first-order partial differential equations. With no current or charge present, these equations can be decoupled by taking the cross product of equations 2.2 and 2.4 and using the vector identity $\nabla \times (\nabla \times \boldsymbol{V}) = \nabla(\nabla \cdot \boldsymbol{V}) - \nabla^2 \boldsymbol{V}$. The result is two second-order differential equations,

$$\nabla^2 \boldsymbol{E} = \frac{1}{v^2} \frac{\partial^2 \boldsymbol{E}}{\partial^2 t}, \quad \nabla^2 \boldsymbol{B} = \frac{1}{v^2} \frac{\partial^2 \boldsymbol{B}}{\partial^2 t}, \tag{2.5}$$

where $v = (\epsilon_0 \epsilon_r \mu_0 \mu_r)^{-1/2} = cn$ is the speed of the electromagnetic wave, $c = (\epsilon_0 \mu_0)^{-1/2}$ is the speed in vacuum and $n = (\epsilon_r \mu_r)^{-1/2}$ is the refractive index. An optical wave is mathematically described by a scalar function $u(\boldsymbol{r}, t)$ known as a wave function. It must satisfy the wave equation [26],

$$\nabla^2 u = \frac{1}{c^2}\frac{\partial^2 u}{\partial^2 t}. \tag{2.6}$$

For convenience the wave function can be represented by a complex wave function $U(\boldsymbol{r}, t)$ defined by

$$u(\boldsymbol{r}, t) = Re[U(\boldsymbol{r}, t)], \quad U(\boldsymbol{r}, t) = U(\boldsymbol{r})\exp(iwt). \tag{2.7}$$

$U(\boldsymbol{r}, t)$ must also satisfy the wave equation. Inserting $U(\boldsymbol{r}, t)$ into the wave equation results in a differential equation for the complex amplitude $U(\boldsymbol{r})$ known as the Helmholtz equation [27],

$$\nabla^2 U(\boldsymbol{r}) + k^2 U(\boldsymbol{r}) = 0, \tag{2.8}$$

where $k = w/v$.

The simplest solution to the wave equation, equation 2.6, is the plane wave generally written as

$$U(\boldsymbol{r}, t) = U(\boldsymbol{r})\exp(iwt) = A_0\exp(i(wt - \boldsymbol{k}\cdot\boldsymbol{r})), \tag{2.9}$$

where A_0 is a time- and spatial independent complex amplitude.

2.2 Fresnel equations

In addition to describing how electromagnetic waves propagate in a medium, Maxwell's equations also describe how waves are transmitted through or reflected at an interface between two media. An electromagnetic wave consists of an electric and a magnetic field propagating with the same frequency and being mutually perpendicular [28]. From equation 2.5 the plane wave solutions are

$$\boldsymbol{E}(z, t) = \boldsymbol{E_0}\exp(i(wt - \boldsymbol{k}\cdot\boldsymbol{r})), \quad \boldsymbol{B}(z, t) = \boldsymbol{B_0}\exp(i(wt - \boldsymbol{k}\cdot\boldsymbol{r})). \tag{2.10}$$

These are monochromatic plane waves of frequency ω. The boundary equations further limit and relate $\boldsymbol{E}$ and $\boldsymbol{B}$ on both sides of an interface between two materials [25],

$$\begin{aligned} \epsilon_1 E_1^{\perp} - \epsilon_2 E_2^{\perp} = 0, \qquad & \boldsymbol{E_1^{\parallel}} - \boldsymbol{E_2^{\parallel}} = 0. \\ B_1^{\perp} - B_2^{\perp} = 0, \quad & \frac{1}{\mu_1}\boldsymbol{B_1^{\parallel}} - \frac{1}{\mu_2}\boldsymbol{B_2^{\parallel}} = 0. \end{aligned} \tag{2.11}$$

The subscript 1 and 2 stands for waves in medium 1 and 2. The boundary equations show that the tangential part of $\boldsymbol{E}$ and the perpendicular part of $\boldsymbol{B}$ are continuous along the surface.

Consider a monochromatic plane wave impinging on an interface between two media. Let $\boldsymbol{E}_i$ be the electric field propagating in medium 1 and being incident on medium 2. Then $\boldsymbol{E}_r$ and $\boldsymbol{E}_t$ denote the reflected and transmitted electric field. The tangential part of the electric fields are then continuous along the surface,

$$\boldsymbol{u_n} \times \boldsymbol{E}_i + \boldsymbol{u_n} \times \boldsymbol{E}_r = \boldsymbol{u_n} \times \boldsymbol{E}_t, \tag{2.12}$$

where $\boldsymbol{u}_n$ is a unit vector normal to the surface. Using Maxwell's equations, equations 2.1-2.4, the boundary equations, equation 2.11, and the fact that the phases of the three waves must be equal, Snell's law can be derived [29],

$$n_1 \sin\theta_i = n_2 \sin\theta_t. \tag{2.13}$$

The refractive index is denoted n_1 and n_2 for medium 1 and 2 respectively, and θ is the angle between the direction of the wave vector k and the surface normal. Alternatively, Snell's law can be rewritten in terms of the angle α between the wave vector and the surface, see Figure 2.1. Then Snell's law becomes

$$n_1 \cos\alpha_i = n_2 \cos\alpha_t. \tag{2.14}$$

Furthermore, the law of reflection states that $\theta_i = \theta_r$, or $\alpha_i = \alpha_r$. In X-ray physics, α is more conveniently used as the incident angle. This is because the index of refraction n is close to one resulting in small critical angles. α will therefore be used as the incident angle in this thesis unless specified otherwise. The critical angle of which the plane wave is being totally reflected is defined as the incident angle where $\theta_t = 0$ [29],

$$\theta_c = \arcsin\frac{n_2}{n_1}, \quad \alpha_c = \arccos\frac{n_2}{n_1}, \tag{2.15}$$

for waves going to an optically lighter medium. For all incident angles α below the critical angle α_c the plane wave is totally reflected.

Consider a plane wave incident on a non-magnetic dielectric surface such that $\mu_r = \mu_i = \mu_t = \mu_0$, where μ_0 is the permeability of free space, and $\boldsymbol{E}$ being perpendicular to the plane of incidence (s-polarised), as shown in Figure 2.1.

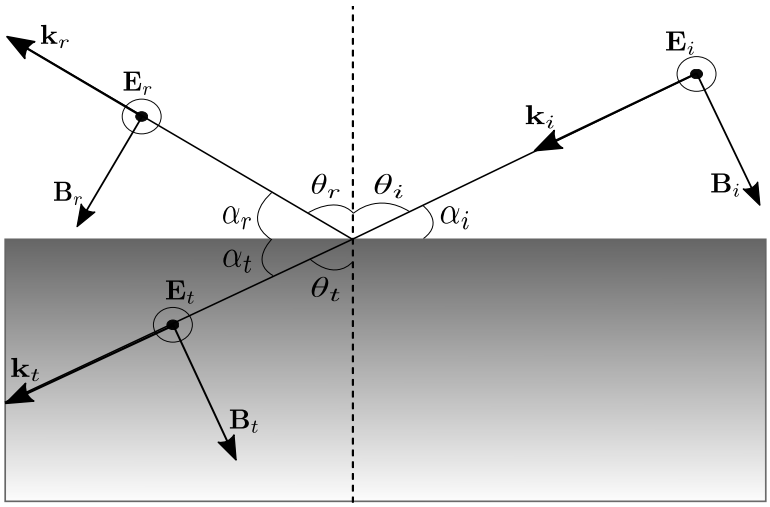

Figure 2.1: The Fresnel geometry of a s-polarised plane wave.

The Fresnel Equations can then be derived from the boundary conditions, equations 2.11, and Maxwell's equations, equations 2.1-2.4 [25; 29] ,

$$r_\perp = \frac{E_{0r}}{E_{0i}} = \frac{n_i \cos\theta_i - n_t \cos\theta_t}{n_i \cos\theta_i + n_t \cos\theta_t} \tag{2.16}$$

and

$$t_\perp = \frac{E_{0t}}{E_{0i}} = \frac{2n_i \cos\theta_i}{n_i \cos\theta_i + n_t \cos\theta_t}. \tag{2.17}$$

In the above equations $r_\perp$ and $t_\perp$ denote the amplitude reflection and transmission coefficients for s-polarized light. For p-polarized light the Fresnel equations for the parallel components of the amplitude reflection and transmission coefficients $r_\parallel$ and $t_\parallel$ become

$$r_\parallel = \frac{n_t \cos\theta_i - n_i \cos\theta_t}{n_t \cos\theta_i + n_i \cos\theta_t}, \tag{2.18}$$

and

$$t_\perp = \frac{2n_i \cos\theta_i}{n_t \cos\theta_i + n_i \cos\theta_t}. \tag{2.19}$$

2.2.1 X-ray regime

The index of refraction in the X-ray regime is conveniently expressed as

$$n = 1 - \delta - i\beta, \tag{2.20}$$

where δ is related to the scattering properties of the medium and is usually in the order of 10^{-5}. β is proportional to the absorption cross section and is usually much smaller than δ [2].

Consider an X-ray beam incident on a medium of refractive index n_2 from vacuum where $n_1 = 1$. The critical angle is small as the deviation of n_2 from unity is small. When the incident angle is close to the critical angle, Snell's law can be expanded giving

$$\alpha_i^2 = \alpha_t^2 + 2\delta - 2i\beta, \quad \alpha_c = \sqrt{2\delta}. \tag{2.21}$$

Similarly, the Fresnel equation of the amplitude reflection coefficient for s-polarized light can be expanded giving

$$r = \frac{\alpha_i - \alpha_t}{\alpha_i + \alpha_t}. \tag{2.22}$$

2.3 Reflection from a film on a surface

While the Fresnel equations derived in the previous section are of great importance, the case of a single surface is for many practical purposes not sufficient. In many cases layered systems are present and scattering from all layer interfaces must be accounted for [30]. In this section, reflection from a film with thickness Δ on a surface will be considered, see

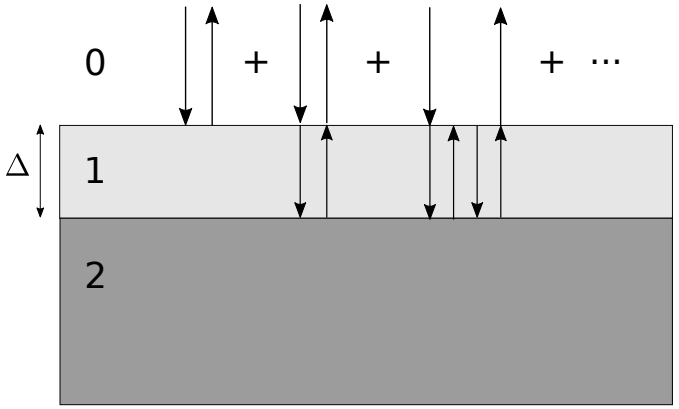

Figure 2.2: Schematic of possible reflections of a slab of finite thickness. The regions 0, 1 and 2 has index of refraction $n_0 = 1.0$, n_1 and n_2 respectively. Layer 1 has thickness Δ while layer 2 has infinite thickness.

Figure 2.2. Medium 0 is considered to be vacuum with $n_0 = 1.0$, while media 1 and 2 are homogeneous with indexes of refraction n_1 and n_2. An X-ray beam incident on a film on a substrate has in principle an infinite series of possible reflections. Three of these reflections are visualized in Figure 2.2. The first reflection possibility visualized in Figure 2.2 is that the beam is entirely reflected at the interface between material 0 and 1 with reflection amplitude r_{01}. Secondly, the beam can be transmitted at the interface 0 to 1 (t_{01}), reflected at interface 1 to 2 (r_{12}) and then transmitted again at interface 1 to 0 (t_{10}). A phase factor of $p^2 = \exp(iQ_1\Delta)$ is needed when adding this reflection possibility. The wave vector transfer Q_1 is defined as $Q_1 = 2k\sin\alpha_1 \approx 2k\alpha_1$, where $\alpha_1 = \alpha_t$. Thirdly, the beam can be transmitted at interface 0 to 1 (t_{01}), reflected at interface 1 to 2 (r_{12}), reflected at interface 1 to 0 (r_{10}), reflected at interface 1 to 2 (r_{12}) and lastly a transmission at interface 1 to 0 (t_{10}). The corresponding phase factor is p^4. Additionally, infinitely many possibilities may be described by combinations of the two reflection amplitudes, r_{01} and r_{12}, and the two transmission amplitudes, t_{01} and t_{10}. The total reflection amplitude coefficient is then

$$r = r_{01} + t_{01}r_{12}t_{10}p^2 + t_{01}r_{12}r_{10}r_{12}t_{10}p^4 + ... \quad . \tag{2.23}$$

Evaluating the geometric series and using $r_{01} = -r_{10}$, the expression for r becomes [2]

$$r = \frac{r_{01} + r_{12}p^2}{1 + r_{01}r_{12}p^2}. \tag{2.24}$$

2.4 Coordinate system

Before moving on to studying GISAXS and later the derivation of the Gaussian beam, the coordinate system used during this thesis must be defined. Figure 2.3 defines the (x, y, z)

coordinate system and the (q_x, q_y, q_z) coordinate system relative to the sample in real and reciprocal space. The z and q_z axes are defined to be parallel to the surface normal.

A beam incident on the sample has for simplicity been chosen to lie in the (x, z)-plane. In the case of specular reflectivity, the scattered beam will also lie in this plane as shown schematically in Figure 2.4. Two additional coordinate systems can be defined, along the direction of the incident and the scattered wave. These are denoted (x_i, z_i) and (x_{sc}, z_{sc}). α_i, α_{sc} is the angle the beam and the x_i, x_{sc} axis makes with respect to the x axis. In this thesis these three coordinate systems will exclusively be used.

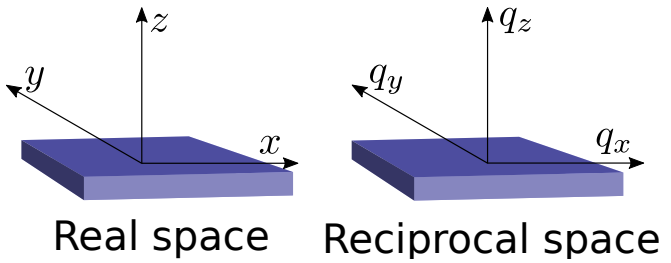

Figure 2.3: A schematic of the coordinate system defining the real space coordinates (x, y, z) and the reciprocal space coordinates (q_x, q_y, q_z) with respect to the sample. The z and q_z axes are parallel to the surface normal.

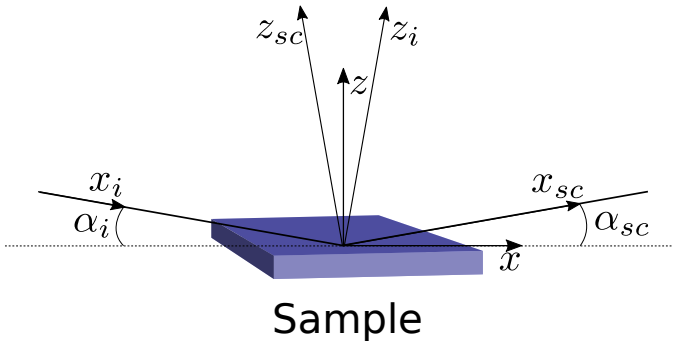

Figure 2.4: A schematic of the coordinate system in specular reflectivity. The incident beam propagates along the x_i axis at an angle α_i with respect to the x axis. Similarily, the scattered beam propagates along the x_{sc} axis at an angle α_{sc} with respect to the x axis.

2.5 GISAXS

In grazing incidence the beam is incident with a small incident angle α_i, generally close to the critical angle. In grazing incidence small-angle X-ray scattering (GISAXS) the in-plane scattering angle 2Ψ with respect to the sample surface is additionally small. GISAXS is used for studying nanoscale structures and the small scattering angle results in large periodic structures being probed in real space [13; 31; 32]. A sketch of the GISAXS

geometry is shown in Figure 2.5. A beam with wave vector $\boldsymbol{k}_i$ is incident with an angle α_i on a material with nanoscale particles on top. As an example, these islands are taken to be spherical. The detector detects the resulting diffraction pattern from the scattered beam of wave vector $\boldsymbol{k}_f$ at an angle α_{sc}. The wave vector transfer$\boldsymbol{q}$ is given by the difference between scattered and incident wave vector, $\boldsymbol{q} = \boldsymbol{k}_f - \boldsymbol{k}_i$, where $|\boldsymbol{q}| = 4\pi/\lambda \sin\theta$ with 2θ being the scattering angle. Figure 2.5A shows the GISAXS setup in the (x, z) plane illustrating where the scattering angle 2θ is defined while Figure 2.5B shows the (x, y) plane defining the in-plane scattering angle 2Ψ.

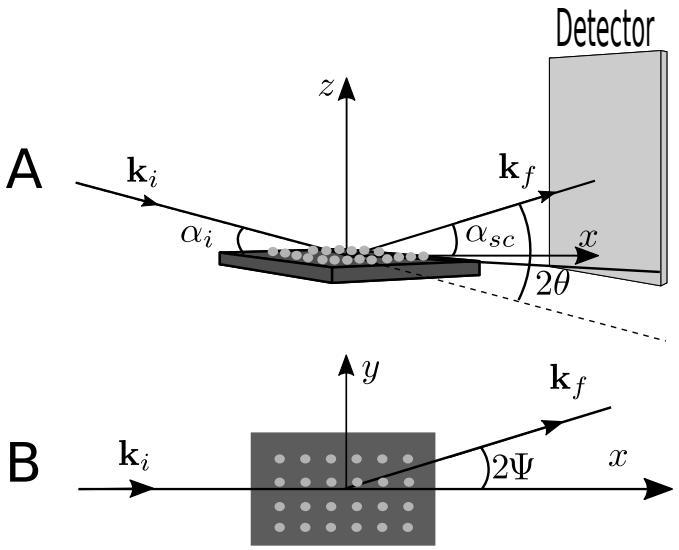

Figure 2.5: A sketch of the GISAXS setup in the A) (x, z) plane and B) (x, y) plane. A wave vector $\boldsymbol{k}_i$ is incident with an angle α_i on spherical islands on a substrate. The detector detects the resulting diffraction pattern from the scattered beam of wave vector $\boldsymbol{k}_f$ and angle α_{sc}. 2Ψ denotes the in-plane scattering angle with respect to the sample surface and 2θ is the scattering angle.

For incident angles below the critical angle, there will be no transmitted wave. This phenomenon is called total external reflection. However, the fields in the medium are nonzero and a so-called evanescent wave travelling parallel to the surface will rapidly be attenuated in z [25]. The evanescent wave will be confined to the top layer and thus enhance the signal-to-noise ratio from the surface. GISAXS is therefore a good technique to investigate morphological properties of nanostructures on surfaces, with sizes from about 1 nm to 1 mm [8; 13].

Having defined the GISAXS geometry and its usage, the focus will now turn to a theoretical treatment of GISAXS. Here, we shall consider one island of a specified shape, for example a sphere or a cylinder, placed on an infinite smooth substrate [8]. The calculation of the scattering cross section in the GISAXS geometry requires the distorted wave Born approximation (DWBA) with multiple scattering events [9] as shown schematically in Figure 2.6.

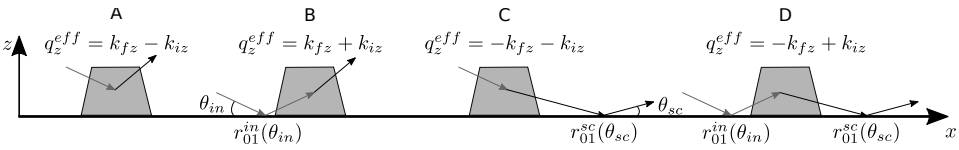

Figure 2.6: Schematic of the four DWBA scattering events on an island [8]. Each event has a corresponding vertical effective wave vector q_z^{eff}.

Figure 2.6 shows four different scattering events all interfering on the island coherently. The first event, Figure 2.6A, is a direct scattering by the island and is equivalent to the first Born approximation. In the second and third event, Figure 2.6B and Figure 2.6C, the incident or scattered beam is reflected off the substrate. In the fourth event, visualized in Figure 2.6D, both the incident and scattered beam are reflected. All four events have a corresponding island form factor $F(\boldsymbol{q}_{\parallel})$ calculated with a vertical effective wave vector transfer q_z^{eff}. The form factor is defined as the Fourier transform of the particle shape

$$F(\boldsymbol{q}) = \int_{S(\boldsymbol{r})} \exp(i\boldsymbol{q} \cdot \boldsymbol{r}) d\boldsymbol{r}. \tag{2.25}$$

Ref. [8] lists several form factor expressions of different geometrical shapes. In this thesis the hemi-spheroid will be studied. Its form factor is given by

$$F_{hsphe}(\boldsymbol{q}, R, W, H) = 2\pi \int_0^H R_z W_z \frac{J_1(\gamma)}{\gamma} \exp(iq_z z) dz \tag{2.26}$$

with

$$R_z = R\sqrt{1 - \left(\frac{z}{H}\right)^2}, \quad W_z = R\sqrt{1 - \left(\frac{z}{H}\right)^2}, \quad \gamma = R\sqrt{(q_x R_z)^2 + (q_y H_z)^2}. \tag{2.27}$$

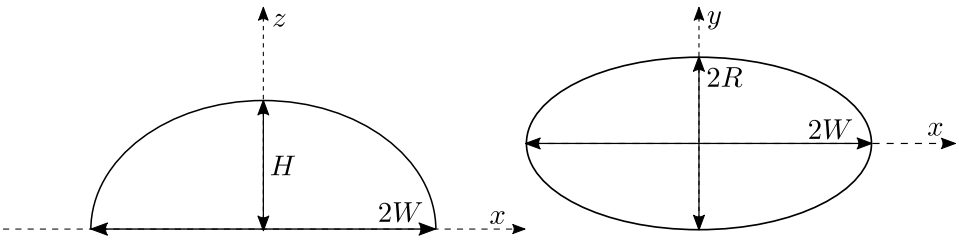

Figure 2.7: Schematic of the hemi-spheroid.

The hemi-spheroid is shown schematically in Figure 2.7. H is the height of the island in the z direction, and $2W$ and $2R$ are the diameters in x and y direction. J_1 is the Bessel function of first order [26]. The volume of the hemi-spheroid is given by $V_{hsphe} = \frac{2}{3}\pi RWH$.

The four scattering events are weighted by the Fresnel reflection coefficients of the corresponding reflections. The DWBA island form factor, or total form factor, $\mathscr{F}(\boldsymbol{q}_{\parallel}, k_{in\,z,0}, k_{sc\,z,0})$, is defined mathematically as

$$\begin{aligned}\mathscr{F}(\boldsymbol{q}_{\parallel}, k_{in\,z,0}, k_{sc\,z,0}) = F(\boldsymbol{q}_{\parallel}, k_{sc\,z,0} - k_{in\,z,0}) + r_{0,1}^{in} F(\boldsymbol{q}_{\parallel}, k_{sc\,z,0} + k_{in\,z,0}) \\ + r_{0,1}^{sc} F(\boldsymbol{q}_{\parallel}, -k_{sc\,z,0} - k_{in\,z,0}) + r_{0,1}^{in} r_{0,1}^{sc} F(\boldsymbol{q}_{\parallel}, -k_{sc\,z,0} + k_{in\,z,0}).\end{aligned} \tag{2.28}$$

The wave vector transfer is $\boldsymbol{q} = \boldsymbol{k}_{sc} - \boldsymbol{k}_{in}$ and the Fresnel coefficients in incidence and after scattering on the island are $r_{0,1}^{in}$ and $r_{0,1}^{sc}$. The differential scattering cross section can then be derived to be [8]

$$\left(\frac{d\sigma}{d\Omega}\right) = \frac{k_0^4}{16\pi^2}\left|n_i^2 - 1\right|^2 \left|\mathscr{F}(\boldsymbol{q}_{\parallel}, k_{in\,z,0}, k_{sc\,z,0})\right|^2, \tag{2.29}$$

where n_i is the refractive index of the island. In the specular limit with $q_{\parallel} = 0$, $k_{sc\,z,0} = -k_{in\,z,0}$ and $r_{0,1}^{in} = r_{0,1}^{sc} = r_{0,1}$ the DWBA island form factor reduces to

$$\mathscr{F}(\boldsymbol{q}_{\parallel}, k_{in\,z,0}, k_{sc\,z,0}) = F(0, 2k_{-in\,z,0}) + 2r_{0,1}F(0,0) + r_{0,1}^2 F(0, 2k_{in\,z,0}), \tag{2.30}$$

where $F(0,0)$ following equation 2.25 gives the volume of the particle. In the limit of small $k_{in\,z,0}$ for the hemi-spheroid, $F(0, 0 \pm 2k_{in\,z,0})$ becomes

$$F(0, 0 \pm 2k_{in\,z,0}) = V_{hsphe}(1 \pm \frac{3}{4}iHk_{in\,z,0} - \frac{2}{5}H^2 k_{in\,z,0}^2). \tag{2.31}$$

The differential cross section in the specular limit with additional small $k_{in\,z,0}$ is then

$$\begin{aligned}\left(\frac{d\sigma}{d\Omega}\right) = \frac{k_0^4 V_{hsphe}^2}{16\pi^2}\left|n_i^2 - 1\right|^2 \\ \cdot\left|2r_{0,1} + (1 + r_{0,1}^2)\left(1 - \frac{2}{5}H^2 k_{in\,z,0}^2\right) + \frac{3}{4}iHk_{in\,z,0}(r_{0,1}^2 - 1)\right|^2\end{aligned} \tag{2.32}$$

As the differential cross section is proportional to the intensity provided the geometry of the instruments are unchanged [2; 8], we take for the general case

$$r \propto \frac{k_0^2}{4\pi}\left(n_i^2 - 1\right)\mathscr{F}(\boldsymbol{q}_{\parallel}, k_{in\,z,0}, k_{sc\,z,0}). \tag{2.33}$$

In the limit of wide incident and scattered angles, $\theta_{in}, \theta_{sc} > \theta_c$, the Fresnel reflectivities become small. The three latter terms in the DWBA form factor that are multiplied with reflectivity coefficients, see equation 2.28, are negligible. The first term is then dominant resulting in the first Born approximation (BA) being valid [9].

2.6 Coherence

The superposition of waves with different frequencies and points of origin deviates from a plane wave in two ways. Firstly, the beam will not be perfectly monochromatic. Secondly, the beam will not propagate in a well-defined direction. These deviations can be described mathematically through the terms longitudinal and transverse coherence lengths [2]. The longitudinal coherence length, L_L, is defined as the length after which two plane waves of slightly different wavelengths initially in-phase are completely out of phase. When two plane waves have the same wavelength but slightly different propagation directions, then the distance after which they are completely out of phase is called the transverse coherence length L_T.

A coherence volume can be defined as a volume in which the plane waves are approximately in phase and can be given by $L_L L_T^2$. If the coherence volume of a beam is larger than the scattering object, the scattered object will experience an incident beam that is fully coherent. Then the total intensity will be the squared absolute value of the sum of the amplitudes. If the coherence volume is smaller than the scattering object, then different parts of the object will scatter out of phase with each other. The total intensity will then be the incoherent sum of the scattered intensities.

Coherent X-rays have coherent lengths of the order of a few $\mu\mathrm{m}$. Coherent X-ray beams from synchrotron sources are increasingly utilized in spectroscopy and imaging.

Chapter 3

The Gaussian beam

3.1 Mathematical description of the Gaussian beam

An approximate solution of the wave equation, equation 2.6, is the paraxial wave function. Paraxial waves have wavefront normals that are paraxial rays [27], i.e. rays that make a small angle with the optical axis. Mathematically, this is a wave traveling along the optical axis, say the $\hat{\boldsymbol{x}}$ direction, with a complex, slowly varying envelope $A(\boldsymbol{r})$,

$$U(\boldsymbol{r}) = A(\boldsymbol{r})e^{ikx}. \tag{3.1}$$

The envelope $A(\boldsymbol{r})$ is slowly varying in x if the change in $A(\boldsymbol{r})$ within a small distance $\Delta x \sim \lambda$ is much smaller than A itself. This must also hold for the derivative of A,

$$\frac{\partial A}{\partial x} \ll kA, \quad \frac{\partial^2 A}{\partial^2 x} \ll k^2 \frac{\partial A}{\partial x}. \tag{3.2}$$

This leads to a partial differential equation for the envelope $A(r)$ called the Paraxial Helmholtz equation,

$$\nabla_T^2 A + 2ik\frac{\partial A}{\partial x} = 0. \tag{3.3}$$

with $\nabla_T^2 = \frac{\partial^2}{\partial_y^2} + \frac{\partial^2}{\partial_z^2}$ being the transverse Laplacian operator. The most important and realistic solution to the Paraxial Helmholtz equation is the Gaussian beam. The Gaussian beam is of great importance since many types of lasers are Gaussian beams under ideal conditions [27]. The transverse profile of both the field and intensity distribution of a Gaussian beam is that of a Gaussian function centered at the beam axis. The beam is shaped as visualized in Figure 3.1.

The Gaussian beam is characterized by its beam waist w_0 or the beam divergence angle $2\theta_G$, which are related through

$$2\theta_G = \frac{4\lambda}{\pi w_0}. \tag{3.4}$$

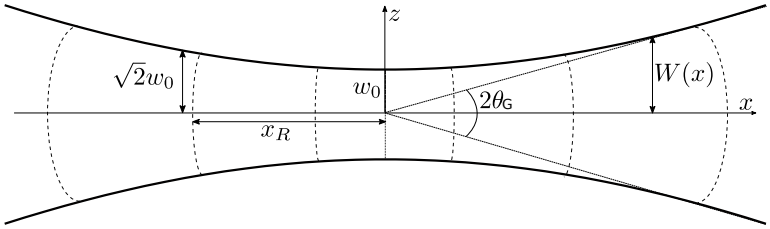

Figure 3.1: A schematic of the Gaussian beam. The beam is propagating in the $\hat{x}$ direction with wave fronts marked by dotted lines. The beam waist w_0 is the half distance at the centre where the beam is the narrowest. The width at any position x is $W(x)$ and the Rayleigh range x_R is defined as the distance at which the width is $\sqrt{2}$ of the beam waist w_0. The beam divergence angle is $2\theta_G$.

The inverse proportionality between the beam waist w_0 and the beam divergence angle $2\theta_G$ means that squeezing the beam waist results in increased beam divergence. Furthermore, the width $W(x)$ at any point x depends on w_0 and the distance x from the center from which w_0 is defined,

$$W(x) = w_0\sqrt{1 + \left(\frac{x}{x_R}\right)^2}, \tag{3.5}$$

where x_R is the Rayleigh range, $x_R \equiv w_0^2\pi/\lambda$. Moreover, the wavefronts are nearly planar in the vicinity of the beam waist w_0. As visualized by the dotted lines in Figure 3.1 the wavefronts gradually curve further away from the beam waist. The radius of curvature of the wavefronts is given by

$$R(x) = x\left(1 + \left(\frac{x}{x_R}\right)^2\right). \tag{3.6}$$

The complex field amplitude of the Gaussian beam satisfying equation 3.1 and 3.3 is given by [27]

$$U(r) = A_0\frac{w_0}{W(x)}\exp\left(-\frac{\rho^2}{W(x)^2}\right)\exp\left(-ikx - ik\frac{\rho^2}{2R(x)} + i\xi(x)\right), \tag{3.7}$$

where $\rho = \sqrt{y^2 + z^2}$ and $\xi = \arctan(x/x_R)$. The corresponding intensity $I(\rho) \propto |U(r)|^2$is at any point x a Gaussian function of the radial distance ρ, as illustrated in Figure 3.2. Figure 3.2A shows the intensity distribution in a plane of constant x, with $\hat{\boldsymbol{x}}$ directed out of the paper. Figure 3.2B shows the intensity distribution of Figure 3.2A as a function of the distance ρ to its centre, a Gaussian function. The beam waist w_0 is recognized as the lateral position at which the intensity and amplitude drop to e^{-2} and e^{-1}, respectively, of their on-axis values.

The Gaussian beam can be described as a superposition of plane waves by a method called the angular decomposition method. How much each plane wave contributes to the total Gaussian beam is described by its angular spectrum, which is given by a Gaussian

function. The relationship between a spatial Gaussian function and its corresponding angular spectrum is

$$f(\rho) = \exp\left(-\frac{\rho^2}{w_0^2}\right), \quad \hat{f}(k) = w_0\sqrt{\pi}\exp\left(-\frac{k^2 w_0^2}{4}\right) \tag{3.8}$$

where $\hat{f}(k_x, k_y)$ is the angular spectrum of $f(\rho) = f(x, y)$ and w_0 is the waist of the Gaussian function related to the divergence of the Gaussian beam by equation 3.4.

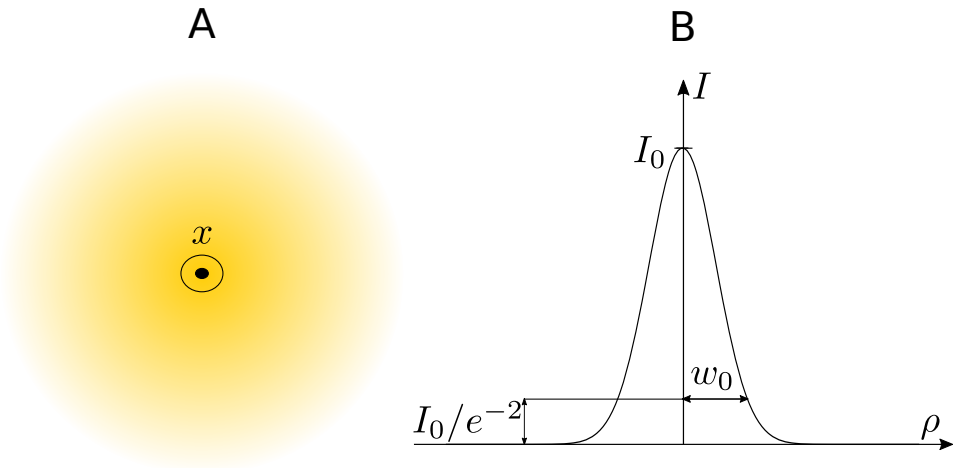

Figure 3.2: A) A Gaussian beam as seen perpendicular to the optical axis ($\hat{x}$ directed out of the paper). B) Intensity distribution of a Gaussian beam.

3.2 Analytical model for reflection of a gaussian beam

In this section a 2D analytical model will be derived for the reflection of a one-dimensional Gaussian beam. Previous research has extensively used the angular decomposition method for studying e.g. the reflection from a dielectric slab [33; 34] and the Goos-Hänchen shift [15]. However, Ref. [16] argues that in the interference region for grazing incidence the reflected and incident field will interfere. The total field close to the reflecting surface will then be a superposition of the two fields. Nevertheless, as we are only interested in the reflected field far away from the reflecting surface, the attention further on will be on the reflected beam. The beam will be assumed to be one-dimensional as well as s-polarized. However, p-polarization can be discussed similarly [16].

Consider a Gaussian beam incident on a surface with incident angle α_0 as illustrated by the red drawing in Figure 3.3. The reflecting surface is along the x-axis and the incident beam can be described in the (x_i, z_i) coordinate system as mentioned in section 2.4. The beam waist, as defined by equation 3.4, is a distance h along the x_i-axis and is considered to be where the beam is launched from. The scattered beam is described in the (x_{sc}, z_{sc}) coordinate system and is drawn in blue in Figure 3.3. The scattered beam is also drawn

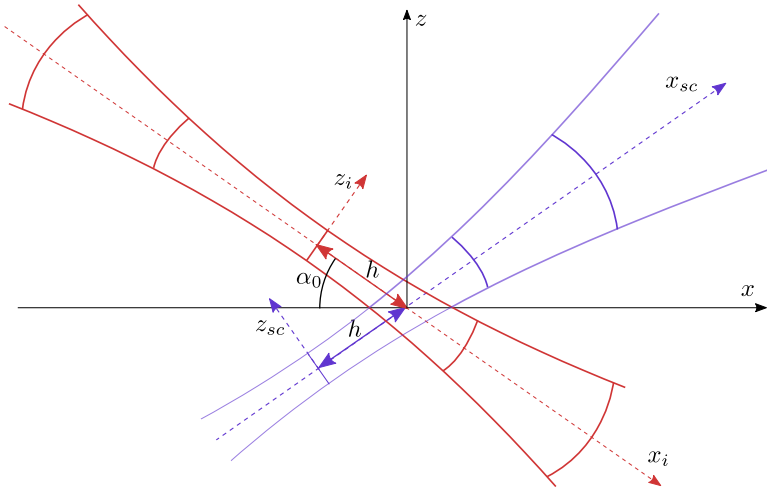

Figure 3.3: An incoming Gaussian beam with incident angle α_0 is described in the coordinate system (x_i, z_i) and is plotted in red. Similarly, the reflected beam is described in the coordinate system (x_{sc}, z_{sc}) and is plotted in blue. The beam waist is at a distance h along the x_i-axis. Inside the reflecting material the reflected beam can be seen as a mirror-image to the incident beam and is marked in weaker lines to show where h is relative to x_{sc}. The wavefronts are visualized.

inside the reflecting material to illustrate where the beam waist is relative to the x_{sc} axis and can be seen as a mirror-image to the incident beam [16].

Along the launching plane the electrical field of the Gaussian beam is described by the distribution $\exp\left(-z^2/w_0^2\right)$. Its corresponding angular spectrum $f(k_z)$ at the plane $x_i = 0$ is then

$$f(k_z) = \sqrt{\pi} w \exp\left(-w_0^2 k_z^2/4\right), \tag{3.9}$$

where k_z is the transverse wave vector of the plane-wave component. A critical wave vector k_{z0} is defined as parallel to the reflecting surface, $k_{z0} = k_0 n_1 \sin\alpha_0$. Here k_0 is the wave vector in vacuum and α_0 is the incident angle of the Gaussian beam defined by its optical axis as seen in Figure 3.3.

The incoming optical field is given by

$$E_i(x,z) = \frac{1}{2\pi}\int_{-\infty}^{\infty} f(k_z)\exp\left(-ik_z z - i\sqrt{k_0^2 n_1^2 - k_x^2}(x-h)\right)dk_z, \tag{3.10}$$

while the reflected optical field is given by

$$E_r(x,z) = \frac{1}{2\pi}\int_{-\infty}^{\infty} f(k_z) r(k_z)\exp\left(-ik_z z - i\sqrt{k_0^2 n_1^2 - k_z^2}(x-h)\right)dk_z. \tag{3.11}$$

$r(k_z)$ is an amplitude reflection coefficient for a plane wave with a transverse wave vector k_z, to be discussed below.

Calculating the field distribution from the integral in equation 3.11 is numerically costly, so we will deduce the angular spectrum of the optical field. The connection between the optical field and its angular spectrum is given by a Fourier transform,

$$E(x,z) = \int_{-\infty}^{\infty} g(k_z, x) \exp(-ik_z z) dk_z, \tag{3.12}$$

which in turn determines the angular spectrum to be

$$g(k_z, x) = f(k_z) r(k_z) \exp\left(-i\sqrt{k_0^2 n_1^2 - k_z^2}(x-h) \right). \tag{3.13}$$

The resulting optical field can then be found by taking the Fourier transform of equation 3.13.

When the reflecting surface is an interface between two linear and semi-infinite media, $r(k_x)$ becomes the Fresnel amplitude reflection coefficient, equation 2.16. Each plane wave component will then be reflected according to the Fresnel amplitude reflection coefficient, as visualized in Figure 3.4A for three selected plane wave components. Each plane wave will have an inherent incident angle $\alpha_i(k_z)$ which relates to the plane wave component k_z as follows

$$\alpha_i(k_z) = \pi/2 + \arccos\left(\frac{k_z}{k_0 n_1}\right) + \alpha_0. \tag{3.14}$$

Equation 3.14 can be derived from Figure 3.3 [35]. The total reflected Gaussian beam will then be a sum over the reflected plane wave components, as given by equation 3.11.

To extend our study from a linear reflecting surface to a multilayered structure, we propose that each plane wave component will be reflected according to the reflection amplitude of a multilayered structure derived in section 2.3, equation 2.24. This is visualized in Figure 3.4B for two selected plane wave components. Compared to Figure 2.2 only two possible reflections for each plane wave component are shown. Similar to the case of one interface above, the total reflected beam will be a sum over the reflected plane wave components. This can be generalized to the GISAXS geometry and other reflecting surfaces, and will be discussed later in this thesis.

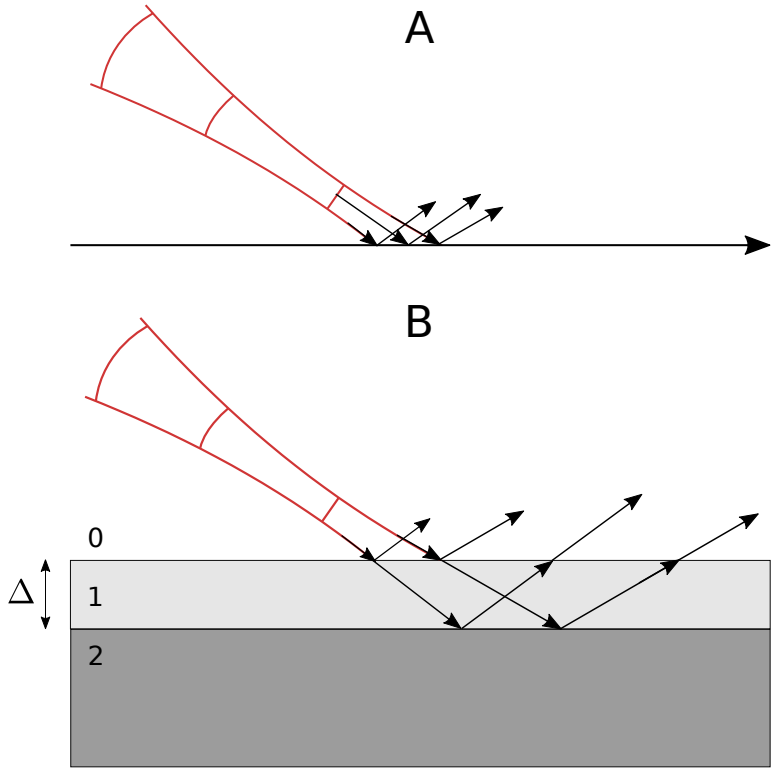

Figure 3.4: An incoming Gaussian beam on a reflecting surface. The reflection of a number of plane wave components is shown to visualize how the reflected Gaussian beam is a sum over the reflected plane wave components. A) The reflecting surface is an interface between two media. B) The reflecting surface consists of a thin film with thickness Δ on a substrate surrounded by vacuum.

Chapter 4

Phase reconstruction

In scientific fields such as optics, X-ray crystallography, X-ray diffraction and electron diffraction only the intensity of a scattered beam can directly be measured, resulting in loss of essential information regarding the phase [22]. This is known as the phase problem.

4.1 Coherent X-ray diffraction

An inverse Fourier transform of a diffraction pattern will not produce an image of the electron density because of the phase problem. However, if the imaged object is small and is fully illuminated with coherent radiation, the phase can be found numerically from the diffraction pattern [2]. This imaging technique is known as coherent X-ray diffraction imaging (CXDI) and has been shown to work on both non-crystalline and crystalline materials [2]. Coherence is required in both the longitudinal and transverse directions, see section 2.6. The required coherence lengths limit the maximum flux accessible in a CXDI experiment to a value proportional to the brilliance of the source [36]. When the beam is sufficiently coherent, the diffraction pattern will show a graininess known as a speckle pattern [37].

Generally, diffraction experiments detect the interference of scattered waves. In incoherent systems, statistically meaningful information is found by taking the ensemble average over numerous local configurations [36]. In other words, the measured intensity is found by summing the intensity contributions from all coherent sub-volumes. However, in a CXDI experiment the measured diffraction signal is simply the magnitude squared of the scattering amplitude, obtained by summing the amplitude contributions from the entire sample. This is the essential point of CXDI. The direct summation over all scattering atoms is given by

$$A_{sc}(\boldsymbol{q}) \propto \sum_j f_j \exp(i\boldsymbol{q} \cdot \boldsymbol{r}_j) \tag{4.1}$$

where f_j is the form factor of atom j. The positions of the atoms are denoted by $\boldsymbol{r}_j$ and the summation is over all atoms within the illuminated volume. The intensity given by

$$I(\boldsymbol{q}) = |A_{sc}(\boldsymbol{q})|^2, \tag{4.2}$$

is then observable.

A CXDI experiment relies on oversampling to be able to retrieve the phase information. It can be shown that if the diffraction pattern can be sampled at half the Nyquist frequency, i.e. oversampled, then it is possible to recover information on both $|A(\boldsymbol{q})|$ and its phase [2]. When imaging isolated objects, an interpretation of the oversampling is that it corresponds to surrounding the sample with a region of zero density. When this region is larger than the region of non-zero density, the phase information can be retrieved [38]. An oversampling ratio σ can be defined as the total area divided by the area of the non-zero density. When $\sigma > 2$ the problem is in principle solvable [17].

CXDI with oversampling can be proven to have a unique solution in 2D and 3D, but in 1D the problem is more diffcult [2; 39]. There exists several numerical algorithms that incorporate oversampling as real-space constraints and applies them in different ways. The Gerchberg-Saxton algorithm, also known as the error-reduction algorithm, is an example of a converging algorithm [21]. Gerchberg and Saxton wrote their algorithm in the 1980s, the first efficient solution to the phase problem [24]. The algorithm will be explained in detail below.

4.2 Coherent X-ray diffraction on a rough surface

For simplicity, we consider only one kind of atom with form factor f. The height of the surface can be defined as a height function, $z = h(x, y)$, where z is perpendicular to the surface as illustrated in Figure 4.1. The scattering amplitude can then be written as [36]

$$A_{sc}(\boldsymbol{q}) \propto F_{CTR}(q_z) \sum_j \exp\left(iq_x x_j + iq_y y_j + iq_z h(x_j, y_j)\right). \tag{4.3}$$

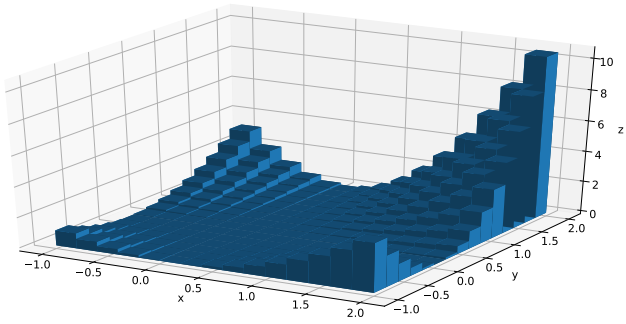

Figure 4.1: An example of a height function, $z = h(x, y)$, with z parallel to the surface normal.

where the summation is now over columns of equally spaced atoms. The summation in the z direction is the same for all columns and is reduced to $F_{CTR}(q_z)$. $F_{CTR}(q_z)$ is known from the analysis of crystal-truncation rods (CTR),

$$F_{CTR}(q_z) = f\left(1 - \exp(-iq_z a_3)\right)^{-1}, \tag{4.4}$$

with a_3 being the vertical lattice spacing. Its amplitude is large close to Bragg peaks in q_z and gets considerably smaller further away [36]. $F_{CTR}(qz)$ will not be discussed further since it in reflectivity falls off as q_z^{-2} close to the origin of reciprocal space. The second factor in equation 4.3 is known as the speckle amplitude and can be rewritten as

$$A(\boldsymbol{q}) = \int\int_{\Omega} \rho(x,y) \exp(iq_x x + iq_y y) dxdy, \tag{4.5}$$

with

$$\rho(x,y) = \exp(i\phi(x,y)), \quad \phi(x,y) = q_z h(x,y). \tag{4.6}$$

The illuminated region, denoted Ω, is finite and depends on the beam width, or the aperture, and the incident angle. In the case of surface CXDI the phase $\phi(x,y)$ can be interpreted as the amount the incident beam at position (x, y) is phase shifted and will depend on the height function $h(x,y)$.

4.3 Reconstruction of surface morphology from 1D speckle pattern

In CXDI reflectivity experiments the sample is measured at grazing incidence. The footprint of the beam on the sample surface will as a result be highly elongated, as visualized in Figure 4.2. The incoming beam is a square beam with dimensions $d \cdot d$ and is for simplicity assumed to be parallel. In Figure 4.2 the probed region is marked darker than the rest of the sample and has length L in the x-direction and d in the y-direction. In grazing incidence $L >> d$ and the problem can then be considered one-dimensional, motivated by Refs. [36] and [40]. The results may be generalized to the 2D case [36].

For an one-dimensional sample the speckle amplitude is defined from equation 4.5 as

$$A^{\text{1D}}(q_x)|_{q_z} = \left|A^{\text{1D}}(q_x)\right| \exp(i\alpha(q_x)) = \int_{-L/2}^{L/2} \rho_0(x) \exp(-iq_x x) dx, \tag{4.7}$$

with density $\rho_0(x)$ and its phase $\phi(x)$ defined as [36]

$$\rho_0(x) = \exp(i\phi(x)), \quad \phi(x) = q_z h(x). \tag{4.8}$$

The height function, or the surface morphology, is given by $h(x)$. Figure 4.3 shows a schematic of the 1D sample. The illuminated area, or the footprint L, relates to the width of the beam d and the incident angle α_i as $L = d/\sin(\alpha_i)$.

When applying iterative algorithms, constraints are needed for convergence. In the present case, an intensity of zero outside of the footprint is enforced as a real-space constraint. We therefore define an illumination filter function [36], $B(x)$, which can conveniently be defined as a product of two Fermi functions,

$$B(x) = f(x - L/2) f(-x - L/2), \tag{4.9}$$

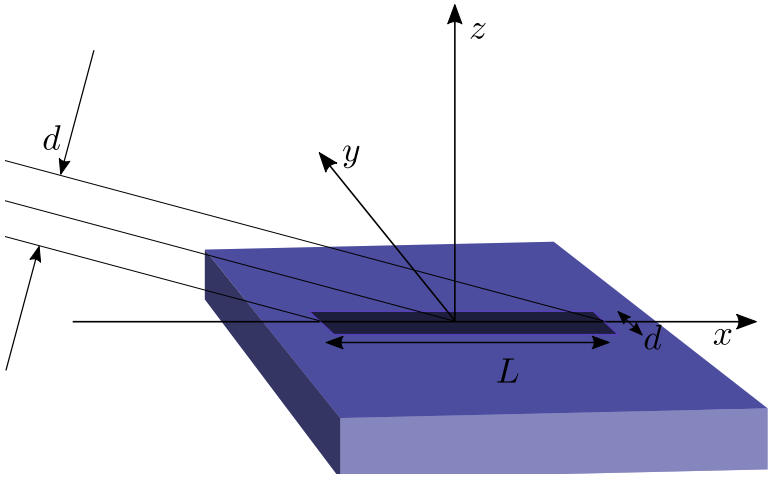

Figure 4.2: An incident square beam with dimensions $d \cdot d$. For simplicity a parallel beam is assumed. The probed sample region is marked as a dark region with length L in the x direction and d in the y direction. The incident beam is arranged at grazing incidence resulting in $L >> d$.

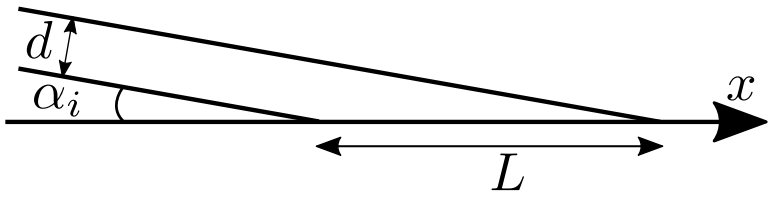

Figure 4.3: Schematic of the 1D sample. The footprint of the beam is denoted L and is given by the incident angle α and the width of the beam d.

where the Fermi function is $f(x) = 1/[1 + \exp(x/w)]$. w determines the sharpness of the edge. Having defined $B(x)$ we can extend the integral in equation 4.7 to infinity,

$$A^{\text{1D}}(q_x) = \int_{-\infty}^{\infty} \rho(x) \exp(-iq_x x) dx, \tag{4.10}$$

with the modified phase function

$$\rho(x) = \rho_0(x)B(x) = B(x) \exp(i\phi(x)). \tag{4.11}$$

The intensity is invariant given a constant offset in the phase $\phi_\delta = \phi + \delta\phi$. The new speckle amplitude will then be

$$A_\delta(q_x) = \exp(i\delta\phi)A(q_x), \tag{4.12}$$

which clearly gives an unchanged intensity, $I_\delta(q_x) = I(q_x)$.

4.4 Gerchberg-Saxton algorithm

The Gerchberg-Saxton algorithm was originally developed for reconstructing the phase from two intensity measurements [23; 41]. Having two intensity measurements means that measured data or information is known *a priori* in both the object and Fourier domain, $|f(\boldsymbol{r})|$ and $I(\boldsymbol{q})$ respectively [21]. In the case of reconstructing surface morphology, as described in the sections above, both $I(q_x)$ and $|\rho(x)| = B(x)$ are known.

The Gerchberg-Saxton algorithm makes use of the fast Fourier transform (FFT) to iterate between real and reciprocal space. Before entering the iterative loop, the phases $\phi(r)$ are randomly generated between $-\pi$ and π. Subsequently, an initial estimate of the density $\rho(r)$ is made. The first step of the loop is to take a FT of $\rho(r)$ giving $A'(\boldsymbol{q})$. Secondly, the constraint in reciprocal space is applied; the speckle amplitude should be equal to the square root of the observed intensity, $|A(\boldsymbol{q})| = \sqrt{I(\boldsymbol{q})}$. Getting a new estimate of the density $\rho'(r)$ from the IFT of $A(\boldsymbol{q})$ is the third step of the iterative algorithm. Fourthly, the real space constraint is applied, $|\rho(r)| = |f(r)|$. The loop is shown schematically in Figure 4.4.

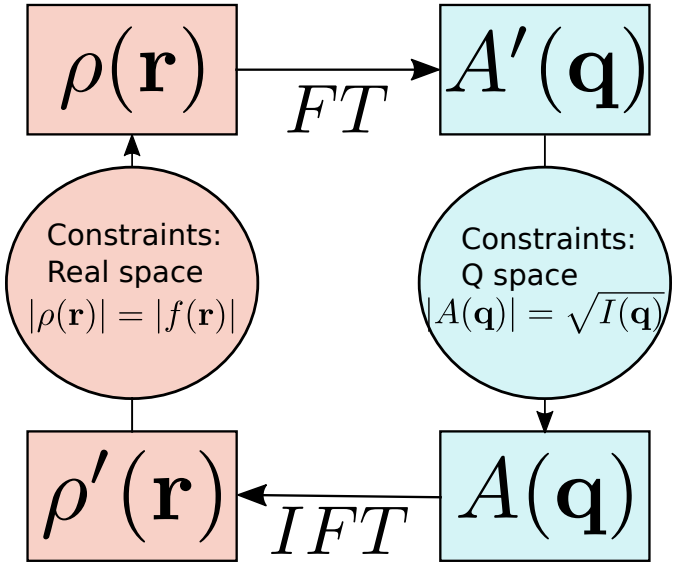

Figure 4.4: A schematic of the Gerchberg-Saxton algorithm. The algorithm iterates between real and Fourier space while applying constraints in both spaces.

The loop visualized in Figure 4.4 continues until it has reached a maximum number of iterations or the algorithm is successful. The algorithm is successful if the error converges to a value close to zero. The error can be calculated using the difference between the absolute value of the estimate and the corresponding constraint in both real and Fourier space,

$$E_k = \frac{\sum \left(\sqrt{I_{exp}} - |A(\boldsymbol{q})|\right)^2}{\sum I_{exp}}, \quad e_k = \frac{\sum \left(|B(r)| - |\rho(r)|\right)^2}{\sum |B(r)|^2} \tag{4.13}$$

The error of each estimate k can be shown to be equal to or less than the previous estimate [21; 24]. The Gerchberg-Saxton algorithm is therefore also known as the error-reduction algorithm. In Ref. [24] Matlab code is provided for the Gerchberg-Saxton algorithm.

The real space constraint $|f(r)|$ can be a positivity constraint or a size constraint [21]. When applying the Gerchberg-Saxton algorithm to reconstruct the 1D surface morphology from the previous section, the real space constraint is given by the illumination filter function $B(x)$. The illumination function ensures that the density amplitude always is one inside the illuminated area.

The question of uniqueness is important when dealing with inverse problems. Ref. [23] recognize two ambiguities, a constant offset in the phase and the ambiguity connected to the complex conjugate. As discussed in the previous section, the intensity $I(\boldsymbol{q})$ will stay unchanged given a constant offset in the phase. Since this also holds for $|\rho(r)|$ only relative phases are meaningful. Moreover, by the properties of the Fourier transform the correct solution $\rho(r) = |\rho(r)| \exp(i\phi(r))$ has a dual solution given by [36]

$$\widetilde{\rho}(r) = \rho^*(-r) = |\rho(-r)| \exp(-i\phi(-r)). \tag{4.14}$$

When studying a rough surface, sections 4.2 and 4.3, the dual solution of the density will then be $\widetilde{\rho}(r) = \exp(-iq_z h(-x, -y))$. In the case of an one-dimensional height profile, section 4.3, the dual height solution will then be reduced to $\widetilde{h}(x) = -h(-x)$.

Without prior knowledge it is impossible to choose between the two solutions. However, in some situations, the problem can be avoided. If the data is measured in the form of a time series or with different incident angles, it is possible under some circumstances to constrain the system to a unique solution [36].

4.5 Other algorithms for the two intensity measurement problem

The speed of convergence of the Gerchberg-Saxton algorithm depends on the type of constraints, but is generally decreasing rapidly in the beginning before stagnating [21]. Stagnation means that the output image changes negligibly after several iterations while not having reached the solution [42]. If the algorithm is initiated with random phases, there is an equal probability that it will reach the correct solution or its dual. When features of both objects are equally present, then the algorithm may stagnate. The algorithm tries to reconstruct both solutions and ends up somewhere in between.

A method that has been proved to converge faster for the two intensity measurement problem is the Hybrid input-output algorithm (HIO) [43]. The algorithm differs only from the Gerchberg-Saxton in the object domain, the left-hand side of Figure 4.4. The system can then be thought of as having an input $\rho(r)$ and an output $\rho'(r)$. Compared to the Gerchberg-Saxton algorithm the input is no longer the current best estimate, it is considered to be a driving function for the next output. The Fourier transform of the output will always satisfy the Fourier-domain constraints. If the output satisfies the object-domain constraints as well, then it is a solution to the problem [21]. The input does not necessarily satisfy the object-domain constraint $|f(\boldsymbol{r})|$. For the case of two intensity measurements the input is given by [44]

$$\rho_{k+1}(r) = \begin{cases} |f(\boldsymbol{r})| \exp(i\theta'_k(r)) & \text{otherwise} \\ \rho_k(r) - \beta\rho'_k(r) & \text{if } r \in \gamma. \end{cases} \tag{4.15}$$

where β is a constant. $|f(\boldsymbol{r})|$ is the known absolute value in the object domain and γ includes all points where $|f(\boldsymbol{r})| = 0$.

Nevertheless, Ref. [44] argues that even the HIO algorithm generally does not converge to a global minimum. They propose an algorithm that combines the Gerchberg-Saxton algorithm and the HIO algorithm to improve the convergence. The new algorithm, which they call the GS/HIO algorithm, begins with n_{GS} iterations of the Gerchberg-Saxton algorithm followed by n_{HIO} iterations of the HIO algorithm. In total there are $N = n_{GS} + n_{HIO}$ iterations. This cycle of Gerchberg-Saxton and HIO iterations, denoted (n_{GS}, n_{HIO}), is then repeated as necessary.

Chapter 5

Results

This chapter will present and discuss the main results of this thesis. First, the propagation of the Gaussian beam will be discussed, including both the intensity and the phase. Second, a Gaussian beam reflecting on a thin film placed on a flat surface will be considered. Third, an island on a substrate in the GISAXS geometry derived in section 2.5 will be explored. Fourth, the Gerchberg-Saxton algorithm will be used in the reconstruction of a one-dimensional surface morphology. Next, the Hybrid input-output algorithm and the combination of the Gerchberg-Saxton and the Hybrid input-output algorithms will be explored and compared with the Gerchberg-Saxton algorithm. Lastly, an attempt will be made at reconstructing an island on a substrate in the GISAXS geometry.

5.1 The Gaussian beam

A Gaussian beam propagating without a reflecting surface will at all times have a transverse intensity distribution of a Gaussian function. However, the shape of the Gaussian function will differ as expected from equation 3.7 in section 3.1. In addition, the curvature of the phase fronts of the Gaussian beam will change as well. Using the equation for an incoming Gaussian beam from section 3.2, equation 3.10, the intensities and wavefronts can be studied at different x planes. As explained in section 3.2, solving the integral is numerically costly, so the angular spectrum $g_i(k_z, x)$ is deduced before solving for the optical field numerically using the FFT. Figure 5.1 shows the intensity and phase of a Gaussian beam at different x planes evaluated numerically from equation 3.10. Figures 5.1A and 5.1B present the relative intensity of the Gaussian beam at $x = 0$ and $x = 0.5$ m, while Figures 5.1C and 5.1D present the phase. The Gaussian beams have beam waist of $w_0 = 3$ µm. Note that in areas where the intensities are zero, the phases are not meaningful.

From the definition of the Gaussian beam in section 3.1, $x = 0$ is where the Gaussian beam is the narrowest. The beam waist can be recognized as the half width of the Gaussian beam when the intensity $I(z)/I_0$ drops to $\exp(-2)$. In Figure 5.1A, the half width is found to be 3.0 µm, consistent with the beam waist w_0 of the Gaussian beam. The half width of the beam at $x = 0.5$ m, Figure 5.1B, is found to be 8.47 µm, in good agreement with the

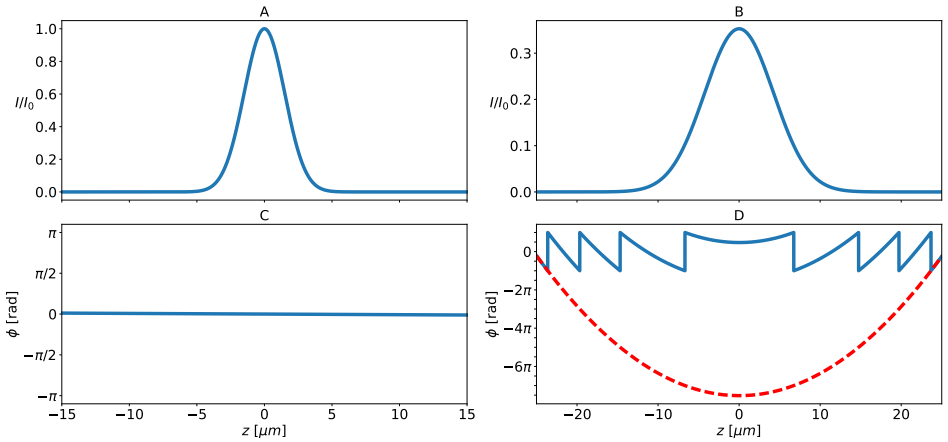

Figure 5.1: Figures A and C show the intensity and phase of a Gaussian beam at the beam waist, $x = 0$. Similarly, Figures B and C show the intensity and phase at $x = 0.5$ m. Note that in the areas where the intensity $I \approx 0$ the phase is not meaningful. The wavelength is $\lambda = 1.5$ Å and the beam waist is $w_0 = 3$ µm.

calculated value $W(x) = 8.5$ µm taken directly from equation 3.5.

The phase in Figure 5.1C is planar, in agreement with $R(x)$ having an infinite radius of curvature from equation 3.6. In Figure 5.1D the blue line presents the phase of a Gaussian beam at $x = 0.5$ m. The red dotted line is the phase plotted in a continuous and smooth curve ignoring the jumps of 2π, the so-called unwrapped phase. The radius of curvature is positive in agreement with $R(x)$, of equation 3.6.

The wavefronts of the Gaussian beam will change with x according to $R(x)$. Figure 5.2 presents the wavefronts of Gaussian beams at selected x planes. The dotted lines have negative x-values and have negative curvature. Similarly, the full lines are calculated from positive x-values and are shown to have positive curvature. The phases are plotted in a region where the corresponding intensity $I/I_0 > 10^{-10}$, indicating the region where the phases are meaningful. For bigger $|x|$ the region in which the phases are meaningful increases indicating that the beam waist $W(x)$ correctly is increasing. From Figure 5.2 it can be seen that the red lines from $|x| = x_R$ have the largest absolute curvature, which is also in agreement with $R(x)$ from equation 3.6.

5.2 Reflection of a Gaussian beam by a thin film

In many practical applications the case of stratified media is present and scattering from all interfaces must be considered [30]. The reflection amplitude for a single thin film of thickness Δ on a substrate was derived in section 2.3, equation 2.24. The multilayered structure is visualized in Figure 2.2. As argued in section 3.1 the reflection amplitude may be inserted directly into the equation for the optical field of a Gaussian beam, equations 3.11 and 3.13.

Figures 5.3A and 5.3B show the reflectivity of a plane wave and of three Gaussian

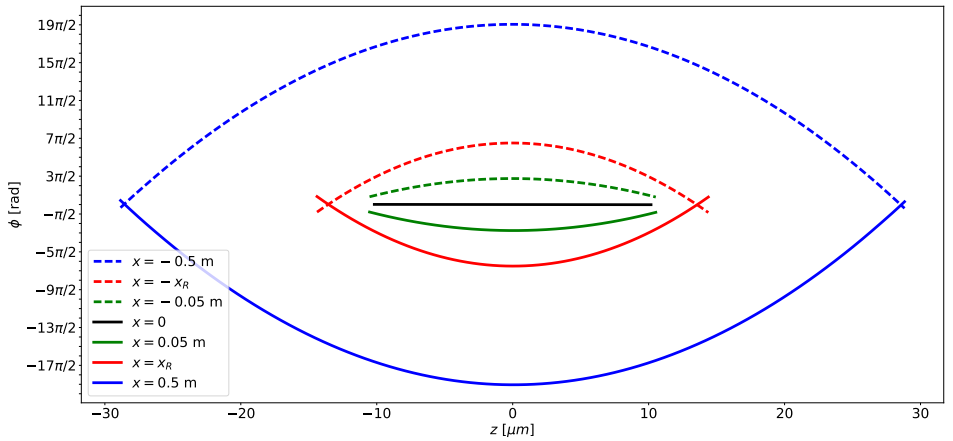

Figure 5.2: Wavefronts of a Gaussian beam at selected x planes. The dotted and full lines correspond to negative and positive x, respectively. Wavefronts with the same colour represent a Gaussian beam at the same $|x|$ and will have equal curvature with opposite sign. The phases are drawn in a region where the corresponding intensity is $I/I_0 < 10^{-10}$ and are therefore terminated at different z. $x = 0$ in black, $x = \pm 0.05$ m in green, $x = \pm x_R \approx \pm 0.19$ m and $x = \pm 0.5$ m in blue.

beams when being reflected by a thin film of thickness $\Delta = 60$ nm on a substrate. The plane wave is plotted in blue and the three Gaussian beams of waist 3 µm, 0.3 µm and 0.1 µm are plotted in orange, green and red, respectively. Figure 5.3A is zoomed in on smaller incident angles α while Figure 5.3B shows a bigger range of incident angles in addition to being logarithmically scaled. Both figures show oscillations corresponding to interference from the two interfaces [2].

The dips at $0.160°$ and $0.240°$ in Figure 5.3A correspond to the critical angles of the thin film and the substrate, marked with black and red dotted lines respectively. The Gaussian with beam waist 3 µm is perfectly following the shape of the reflectivity of the plane wave, including the behaviour around these dips. However, the Gaussian beams with beam waist 0.3 µm and 0.1 µm are smoothing out the sharp dips.

In Figure 5.3B the oscillations caused by film thickness are clearly visible. They are known as Kiessig fringes [2]. Similarly to Figure 5.3A, the Gaussian beams are smoothing out the oscillations causing the oscillations to be barely visible for the Gaussian beam with beam waist 0.1 µm. Its reflectance is more similar to that of a plane wave being reflected on a single, flat surface. A plane wave being reflected on the interface 0 to 2, vacuum to substrate, is shown as black dotted lines in Figure 5.3B as a comparison. Since the Gaussian beam with beam waist 0.1 µm have lost most of the multilayer reflectivity features and show more similarities with a plane wave reflecting on a single interface, it indicates that the Gaussian beam with waist 0.1 µm is not suitable for reflectance measurements of multilayered structures with Δ of the same magnitude.

A Gaussian beam will in the limit of a large beam waist have a narrow angular spectrum where only a few plane wave components have a non-negligible contribution. In this limit, the behaviour of a Gaussian beam should be close to that of a plane wave. The reflectivity

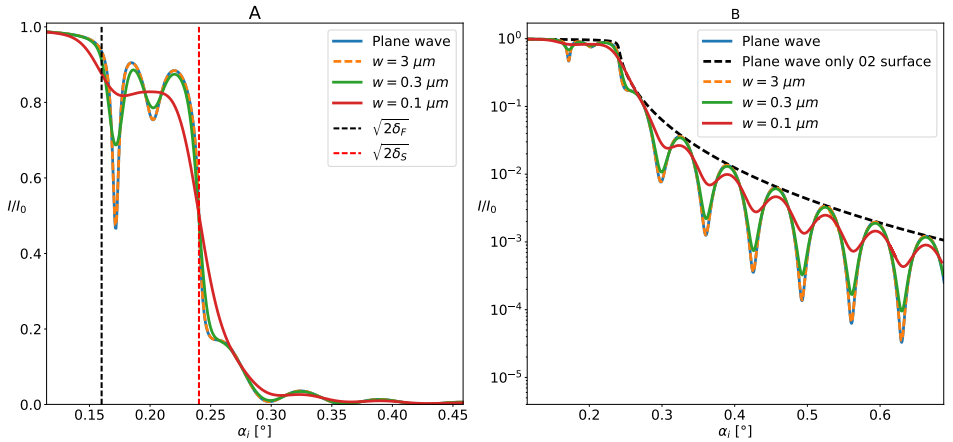

Figure 5.3: Reflectivity of an organic thin film on a glass (SiO_2) substrate as a function of incident angle α_i. A plane wave is plotted in blue and compared with Gaussian beams with beam waist 3 µm, 0.3 µm and 0.1 µm plotted in orange, green and red, respectively. A) The critical angles of the film and substrate marked as black and red dotted lines. B) The reflectivity of a plane wave from vacuum (0) to the substrate (2) is marked as a black dotted line. The vertical axis is logarithmically scaled and is shown for a bigger interval of incident angles in A. The values used in these plots were: $\delta_{Film} = 3.9 \cdot 10^{-6}$, $\beta_{Film} = 2.5 \cdot 10^{-8}$, $\delta_{Substrate} = 8.8 \cdot 10^{-6}$, $\beta_{Substrate} = 11.9 \cdot 10^{-8}$, film thickness $\Delta = 60$ nm and wavelength $\lambda = 1.5$ Å.

of the Gaussian beam with waist $w_0 = 3$ µm corresponds well with the reflectivity of the plane wave, see Figures 5.3A and 5.3B. This similarity indicates that in the boundary of a big beam waist our proposed method of using the plane wave reflection amplitude directly in the equation for the Gaussian beam is valid.

For practical purposes the reflectivity will not reach one at grazing angles. The experimental sample size is usually of the order 1 cm. In addition, beams at laboratories outside of synchrotrons have normally beam waists of magnitude 100 µm resulting in footprints of the order cm. For a beam with beam waist 100 µm incident at $\alpha_i = 0.1°$ the footprint is 5.7 cm, which is of the same order as the sample size. When the footprint is bigger than the sample size, parts of the beam will not hit the sample and will therefore not be reflected. As a consequence the relative intensity I/I_0 will not reach one.

5.3 Scattering of a Gaussian beam on nanoscale islands in the GISAXS geometry

Let us now consider an island of hemi-spherical shape on a substrate in the GISAXS geometry. Section 2.5 outlines the derivation of the DWBA island form factor and the resulting differential cross section. A schematic of the hemi-spheroid is shown in Figure 2.7. The absolute square of the DWBA form factor, $|\mathscr{F}|^2$, is presented in Figure 5.4A and 5.4B. Figure 5.4A ranges over q_z and q_x while in Figure 5.4B q_x is kept constant.

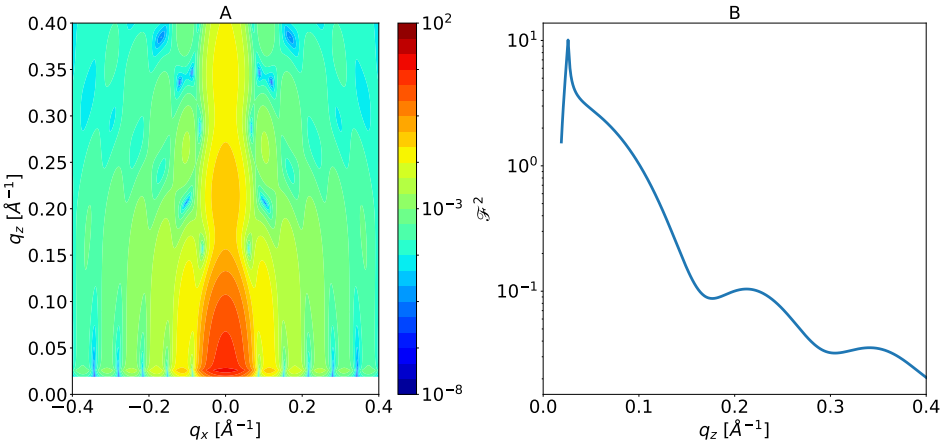

Figure 5.4: The form factor $|\mathscr{F}|^2$ of a island of hemispherical shape. A) The form factor $|\mathscr{F}|^2$ varying with q_z and q_x. B) The form factor $|\mathscr{F}|^2$ as a function of q_z while $q_x = 0$ is kept constant. The following numerical values were used: the height and radius of the hemi-spheroid $R = H = W = 50$ Å, $\alpha_{in} = \alpha_c$, $\lambda = 1.5$ Å and values for the index of refraction of the substrate $\delta_S = 5 \cdot 10^{-5}$ and $\beta_S = 2 \cdot 10^{-8}$.

The symmetry of the hemi-spheroid in the x direction can be found as symmetry in the q_x direction in Figure 5.4A. In the z direction the hemi-sphere is cut off making interference patterns in the form factor that destroys the spherical symmetry. These can, as an example, be observed as dips around ($q_z = 0.15$ Å, $q_x = \pm 0.7$ Å).

Figures 5.4A and 5.4B have a distinct peak at the q_z corresponding to the critical angle of the substrate $\alpha_{sc} = \alpha_c = 0.18°$. According to Ref. [8] this peak is a result of sharp variations between the incident and scattered reflection coefficients, $r^{in}_{0,1}$ and $r^{sc}_{0,1}$, close to the critical angle. Known as the Yoneda peak, its shape is dependent on the incident angle α_{in} and the refractive index of the substrate n_s.

As mentioned in section 2.5 the reflection amplitude is proportional to the square root of the differential cross section given unchanged geometries in the experiment. To compare the scattering of a plane wave with Gaussian beams, the plane wave reflection amplitude is inserted directly into the equations for the Gaussian beam, equations 3.11 and 3.13, as argued in section 3.2. Figure 5.5 compares the intensity of a plane wave with Gaussian beams with beam waist $w_0 = 3$ µm , $w_0 = 0.3$ µm and $w_0 = 0.1$ µm. The Gaussian beam with beam waist 3 µm is plotted with red dots in Figure 5.5 and can be seen to follow the plane wave very well. It therefore suggests that our proposed method for finding the reflection amplitude for the Gaussian beam in the limit of a big beam waist is reasonable.

From the reflectivity of the plane wave and Gaussian beam with beam waist 3 µm in Figure 5.5 the position of the Yoneda peak can be determined. As a result, the critical angle of the substrate can be found. The position of the peak is more difficult to determine for the Gaussian beams of beam waist 0.3 µm and 0.1 µm since the peak is less sharp. Additionally, the oscillations are damped, similarly to the multilayered case.

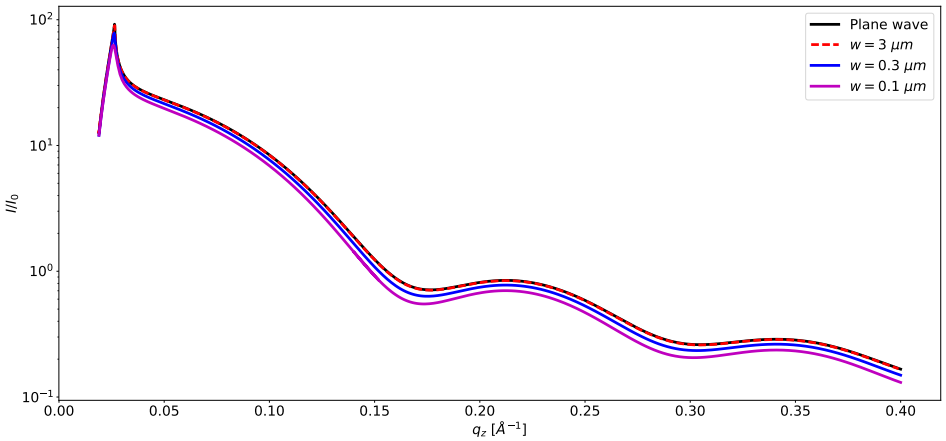

Figure 5.5: Relative intensity of three Gaussian beams and a plane wave. The Gaussian beams are plotted in red, blue and purple having beam waists of $w_0 = 3$ µm , $w_0 = 0.3$ µm and $w_0 = 0.1$ µm respectively. The plane wave is plotted in black. Values used in producing the figure: $\delta_{Island} = 3.9 \cdot 10^{-6}$, $\beta_{Island} = 2.5 \cdot 10^{-8}$, $\delta_{Substrate} = 5 \cdot 10^{-6}$, $\beta_{Substrate} = 2 \cdot 10^{-8}$, and wavelength $\lambda = 1.5$ Å.

5.4 Reconstruction of 1D surface morphology by coherent GISAXS

This section will investigate the Gerchberg-Saxton algorithm for reconstruction of surface morphology in one dimension, as described in sections 4.3 and 4.4. A known surface morphology will generate the speckle intensity $I(q_x, q_z)$ needed for the algorithm. Initiating the algorithm is done with random phases generated from a uniform distribution. The height profile reconstructions from the Gerchberg-Saxton algorithm are calculated with a code based on a script in Ref. [24].

First, the illumination function $B(x)$ defined in section 4.3 is illustrated. Figure 5.6A shows an example of a height profile $h(x)$ of a 1D surface morphology. Figure 5.6B illustrates the illumination function $B(x)$ as defined in equation 4.9 in section 4.3. Combining Figures 5.6A and 5.6B results in Figure 5.6C, the product $B(x)h(x)$.

Second, the relationship between the height function $h(x)$ and the speckle intensity will be studied. The relationship is described by equations 4.2, 4.7 and 4.8 from sections 4.1 and 4.3. Figure 5.7A shows a simulated height profile consisting of a parabolic dip with added noise and the corresponding speckle intensity is shown in Figure 5.7B. The illumination function $B(x)$ was the same as illustrated in Figure 5.6. Note that the footprint L was considered to be constant, i.e. not dependent on q_z. As mentioned in section 4.1, the oversampling ratio must be $\sigma > 2$ to ensure that the speckle pattern is oversampled. We have used $\sigma = 4$ in making Figure 5.7. The difference in the scale of q_z and q_x comes from the grazing incidence making the footprint very elongated compared to the beam waist, as mentioned in section 4.3.

Each $I(q_x)|_{q_z}$ corresponds to a scan over the height profile at a constant angle of

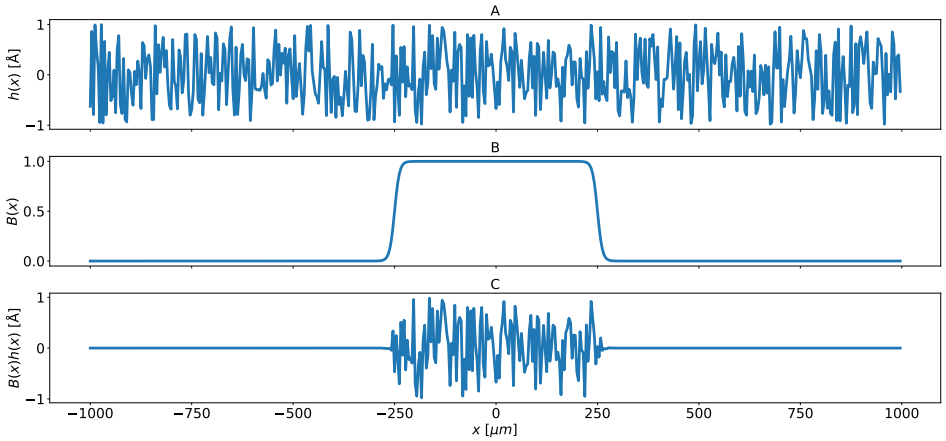

Figure 5.6: A) An illustrative example of a 1D height profile $h(x)$. B) The illumination function $B(x)$ with parameters $w = 6$ µm and $L = 500$ µm. C) The product $B(x)h(x)$.

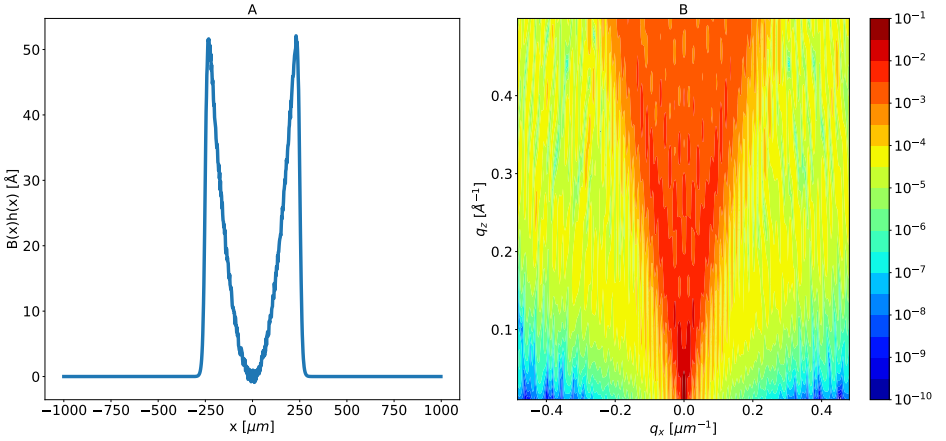

Figure 5.7: A) An example of a height function of parabolic shape added noise. The parameters used in the illumination function $B(x)$ was $w = 6$ µm and $L = 500$ µm. B) The intensity $I(q_x, q_z)$ corresponding to the height profile in A, logarithmically scaled. Note that we have considered the footprint L to be constant.

incidence α_i given by $q_z = \frac{4\pi}{\lambda}\sin(\alpha_i)$. Since $I(q_x)|_{q_z}$ is the input to the Gerchberg-Saxton algorithm, the reconstructions should converge toward the same height profiles. Figure 5.8 compares intensities at different q_z and their reconstructions. Figures 5.8A and 5.8C give the intensities $I(q_x)|_{q_z}$ at $q_z = 0.05$ Å^{-1} and $q_z = 0.10$ Å^{-1}, respectively. Figures 5.8B and 5.8D both show four reconstructions of the height profile. Since the footprint L is dependent on q_z the length of the height profile will vary accordingly. Note that some of the reconstructions are almost identical. Figures 5.8B and 5.8D indeed shows

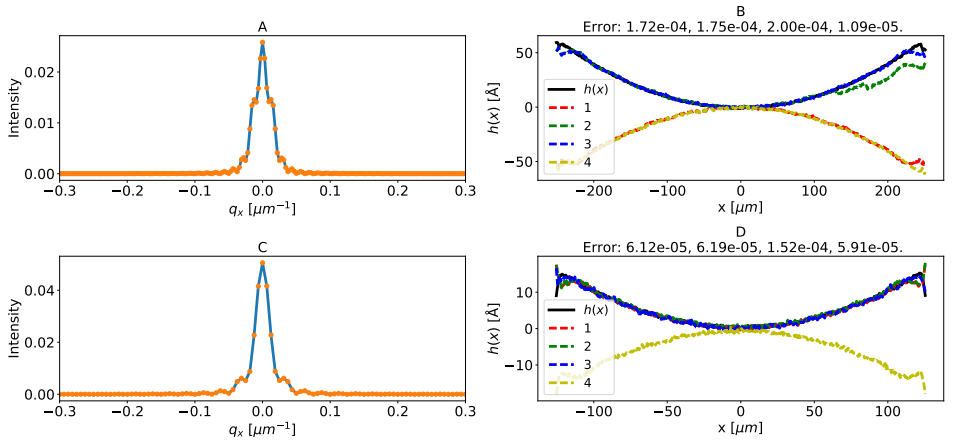

Figure 5.8: A) and D) Intensity $I(q_x)$ at $q_z = 0.05$ Å^{-1} and $q_z = 0.10$ Å^{-1}. B) and D) Height profile reconstructions gained from the intensity measurement in A and C, respectively. Note that the footprint L is dependent on q_z. In addition, some of the reconstructions are almost identical. The parameters used in the illumination function $B(x)$ was $w = 1$ µm.

that by using different $I(q_x)|_{q_z}$ the reconstructions will converge toward the same height profiles.

During the reconstruction process the error was kept track of. The error was calculated using E_k from equation 4.13. In the reconstruction process we sat an error tolerance to be 10^{-10}. However, the calculations were stopped if they reached a maximum number of iterations set to 10^4. The error of each height profile reconstruction in Figure 5.8 is written in the title of each figure. After 10^4 iterations the reconstruction estimates in Figures 5.8B and 5.8D have errors in the order of $10^{-5} - 10^{-4}$.

As mentioned in section 4.4 an ambiguity when doing phase reconstruction is the appearance of a constant offset in the phase. Since the intensity is invariant of this constant offset, we choose to define $\phi(0) = 0$. Another ambiguity mentioned in section 4.4 concerns the dual solution. A symmetrical, one-dimensional height profile will according to equation 4.14 have a dual solution that is the reflection of the correct solution upon the x axis, $\widetilde{h}(x) = -h(x)$. Reconstructions 1 and 4 in Figure 5.8B are clearly converging towards the dual solution. Similarly, reconstruction number 1 in Figure 5.8D converges towards the dual solution.

Figure 5.9 presents two different height profiles with four reconstructions each. In Figure 5.9A the height profile is a Gaussian function while in Figure 5.9B the height profile is a sinusoidal function. Both height profiles have been added noise from a normal distribution. Note that some of the reconstructions are almost identical. The reconstructions in Figures 5.9A and 5.9B have errors in the order 10^{-3} and 10^{-7}, not reaching the previously set error tolerance within the set maximum number of iterations. The convergence will be discussed more later in this section.

The ambiguity regarding the dual solution is a problem for the height profiles in Figure 5.9 as well. Comparing with the known height profile it can be concluded that re-

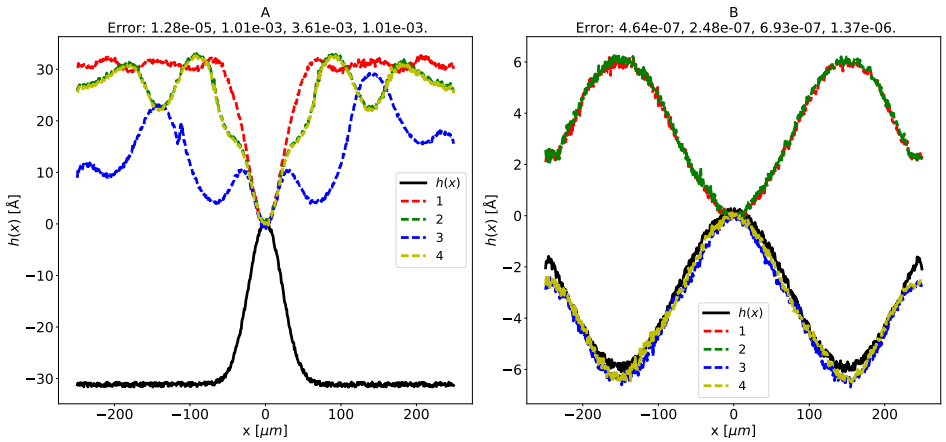

Figure 5.9: Reconstructions from known height profiles. The known height profiles are a A) Gaussian function and a B) sinusoidal function added noise from a normal distribution. Note that some the reconstructions are barely visible behind other reconstructions. $q_z = 0.05$ Å^{-1} and $d = 1$ µm was used for the reconstructions.

construction number 1, 2, 3 and 4 in Figure 5.9A and number 1 and 2 in Figure 5.9B are reconstructions of the dual solution given by equation 4.14.

The error of the reconstructions in Figures 5.8 and 5.9 are varying between 10^{-3} and 10^{-7}. Even lower reconstruction errors might have been reached for a higher number of iterations. A computer with Intel Core i5 CPU with 1.5GHz used approximately 5 seconds to do 10^4 iterations with GS, so the number of iterations can easily be increased. However, the error was seen to stagnate well before 10^4 iterations, so it is therefore believed that the solutions converged towards a local minima. Figure 5.10A shows four height reconstructions for a given parabolic height profile and Figure 5.10B presents their errors. The error of the reconstructions stagnated around 10^{-4}. Note that the difference in the convergence behaviour depends on the initialized phase. The error decreases quickly in the beginning, but stagnate on a nonzero value. This is according to Ref. [24] a weakness in the Gerchberg-Saxton algorithm. Other reconstruction algorithms converge faster [21; 44], which will be investigated in the next section.

In Figures 5.8B, 5.8D, 5.9B and 5.10A the reconstructions have errors between 10^{-4} and 10^{-7}. However, the reconstructions all have the same shape qualitatively, both compared to each other and to the known height solution. Some reconstructions are dual solutions, but as discussed previously in this section and in section 4.4, these are simply the correct height function reflected upon the x axis. A qualitative convergence threshold can therefore be defined to indicate whether a reconstruction has converged to a shape similar to the known height profile or to other reconstructions. Note that similarities to other reconstructions are of great importance as we in most cases do not know the height profile. To determine the qualitative convergence threshold, we study Figure 5.9A as well. Reconstructions 2, 3 and 4 have errors in the order 10^{-3} and are seen to oscillate, being qualitative widely different from the known Gaussian height profile. However, reconstruc-

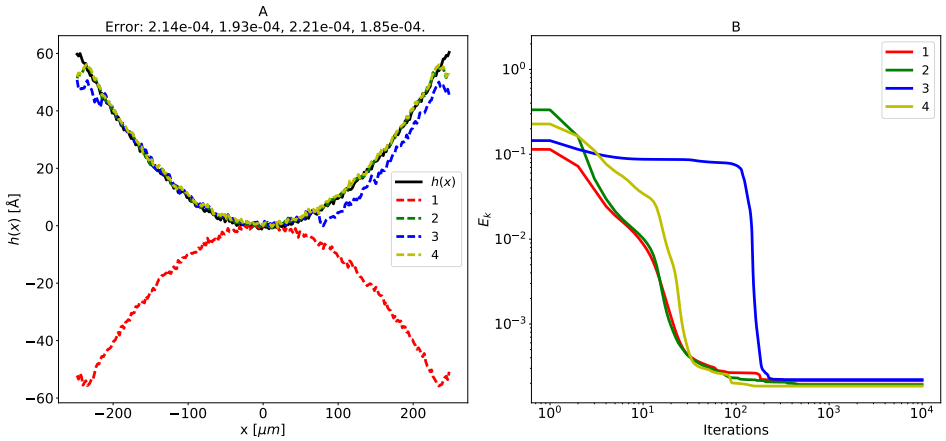

Figure 5.10: A) Presents four reconstructions from a parabolic height profile added Gaussian noise. B) The error of the corresponding reconstructions from Figure A. Note that both axes are logarithmically scaled. The reconstruction cycles were stopped when reaching a maximum number of iterations.

tion number 1 have an error in the order 10^{-5} and is seen to be qualitative similar to the dual solution, obtained from equation 4.14. This indicates that we can define a convergence threshold of 10^{-4}. Reconstructions with error equal to or below the threshold can qualitatively determine the shape of the height profile.

5.5 Comparison with other reconstruction algorithms

Section 5.4 showed that the Gerchberg-Saxton (GS) algorithm often stagnates for a long time before reaching convergence, if convergence is reached at all. Next, we will study the two algorithms introduced in section 4.5 for speeding up the convergence, the Hybrid input-output (HIO) algorithm and the combination algorithm GS/HIO. The algorithms were compared using the error E_k given by equation 4.13. According to Ref. [39] a less loose support, defined by the parameter w in $B(x)$, will improve the reconstruction ability of the iterative algorithms. A stronger support will therefore be used further on.

In the beginning of the previous section, a height function consisting of a parabolic dip with added noise was discussed using the GS algorithm. The same height function was studied when obtaining the reconstruction errors presented in Figure 5.11. Both the GS and HIO algorithms have stagnated with errors around 10^{-2}. HIO is slightly better than GS, however, it still does not generally converge to a global minimum [44]. One cycle of the GS/HIO algorithm consists of 1 iteration of GS followed by 99 with HIO, denoted (1,99). The error from the GS/HIO algorithm is produced by doing a number of cycles. The error from the GS/HIO algorithm decreases rapidly. After 700 iterations the error is oscillating around 10^{-29}, where it can be concluded that the reconstruction algorithm has reached convergence.

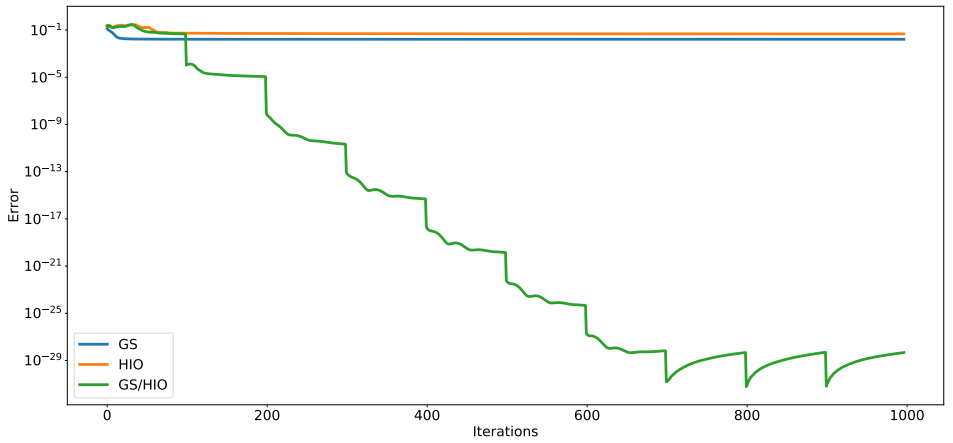

Figure 5.11: Error from reconstruction of a parabolic height function added Gaussian noise. The parameters used in $B(x)$ was $w = 0.01$ µm and $L = 500$ µm. The GS algorithm is plotted in blue, HIO in red and the combination GS/HIO in green. In HIO and GS/HIO the parameter $\beta = 0.5$ was used. One cycle in GS/HIO consisted of one iteration of GS and 99 of HIO, denoted (1,99).

Despite GS and HIO on their own stagnating early, Figure 5.11 shows that a combination of the two produce successful reconstructions. According to Ref. [21] it has been observed that the HIO improves the reconstructed surface morphology rapidly even though the error decreases only slightly. A few iterations of GS following HIO has been found to decrease the error quickly until it becomes more consistent with the quality of the reconstructed surface morphology. Even though Ref. [21] only considers reconstruction from a single intensity measurement, we can clearly see from Figure 5.11 that a few iterations of GS is a key step in decreasing the reconstruction error in the two-intensity measurement problem as well. Each drop in the reconstruction error corresponds to an iteration of the GS algorithm. After 101 iterations the error has dropped to 10^{-6}. Then it slowly decreases for a few iterations until it drops sharply again at the 201st iteration. Since the cycle of iterations consists of 1 iteration of GS and 99 of HIO, the sharp drops indicate when a GS iteration has been completed.

Two questions that arises from Figure 5.11 are i) how changes to the parameter β will affect the convergence and ii) how the behaviour of the error convergence would change if the cycle of iterations of GS and HIO was changed. Figure 5.12 presents the mean and standard deviation of different values of β. The values are calculated from 100 reconstructions initiated with different phases. Figure 5.12 show that both the standard deviation and the mean changes greatly when varying the parameter β. Refs. [21] and [42] conclude that a value of β between 0.5 and 1 produces good results for the problem of one intensity measurement. Ref. [44] assumes that the interval is sufficiently good for the case of two intensity measurements as well. Figure 5.12 indicates that this is partially correct. The error of $\beta < 1.75$ is oscillating rapidly, both with respect to the mean and standard deviation. However, outside of the proposed interval of $(0.5, 1)$ by [42; 21] the error shows a small tendency to increase, especially for $\beta > 1.5$. Using $\beta \approx 2$ even

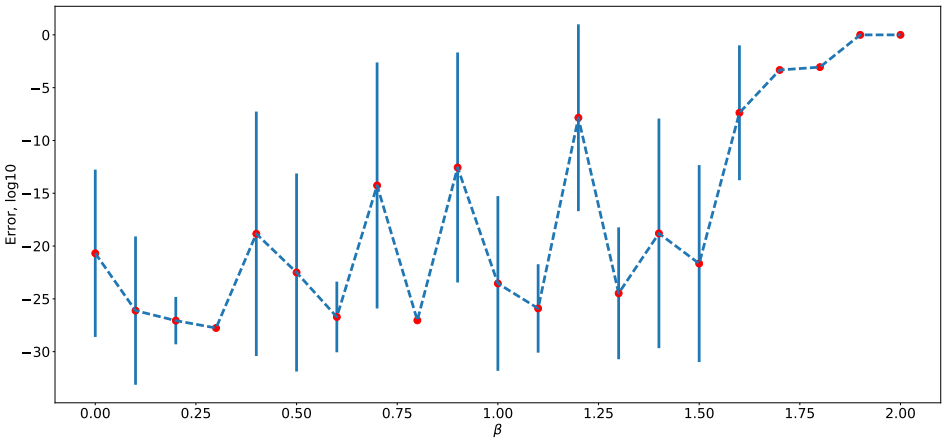

Figure 5.12: The log10 of the error after 1000 iterations of the GS/HIO algorithm with different β. Errorbars in blue show the standard deviation and the red dots present the mean value. The values were calculated from 100 reconstructions with different initial phases. The cycle of iterations in the GS/HIO algorithm was (1,99).

the GS/HIO algorithm will stagnate. Keep in mind that these measurements were done using the GS/HIO cycle (1,99), and that these errors may be specific to this combination. Nevertheless, $\beta = 0.4$ will be used in further calculation since both the mean and standard deviation are very small.

Furthermore, changing the length and composition of the GS/HIO cycle will affect the convergence behaviour. Figures 5.13A and 5.13B presents how the error changes when changing the number of iterations of HIO and GS respectively. Both Refs. [42] and [44] use a number of iterations of HIO between 20 and 100 to solve the one and two intensity problems. This interval is therefore studied in particular, as seen in Figure 5.13A. The changes in both mean and standard deviation are big relative to the changes in Figure 5.12. For example, the mean value for $n_{HIO} = 49$ is approximately 10^{-16} while the standard deviation is $10^{\pm 12}$. Below the mentioned interval the mean and standard deviation increases. Figure 5.13A shows that the best interval for studying the parabolic surface morphology is $n_{HIO} \in (79, 199)$.

Similarly, Ref. [42] suggests an interval of 5 to 10 iterations of GS, n_{GS}, while Ref. [44] concludes that for their case no significant improvement is seen by changing the number of GS iterations while keeping the total number of iterations in the cycle constant. Figure 5.13B studies how the error changes when changing n_{GS} while keeping the cycle length $n_{HIO}+n_{GS} = 100$ constant. The error variation in the mean and standard deviation are huge, varying rapidly from one value of n_{GS} to the next. However, inside the interval $n_{GS} \in (8, 13)$ both the mean and standard deviation are rather small.

In Figures 5.12, 5.13A and 5.13B only one of the parameters β, n_{HIO} and n_{GS} have been changed at a time. Figure 5.12 would look different for a different cycle in the GS/HIO algorithm than (1,99) and similarly for Figures 5.13A and 5.13B. The optimal combination for a parabolic dip using the mentioned parameters in the illumination func-

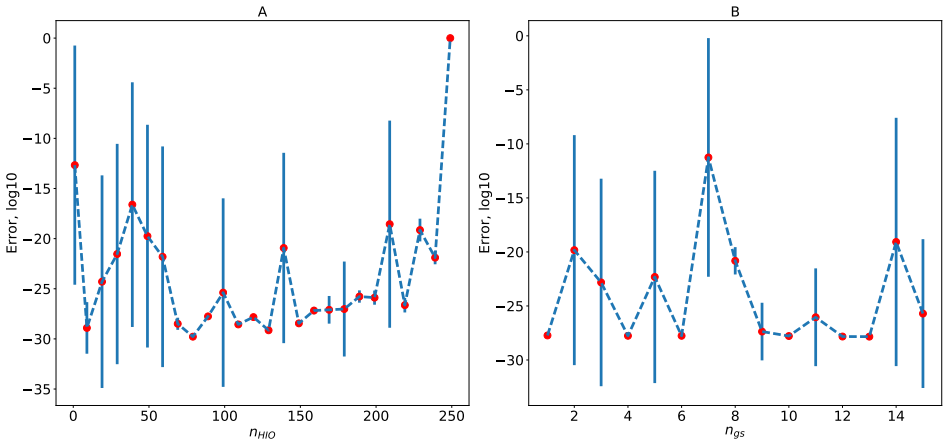

Figure 5.13: The log10 error after 1000 iterations of the GS/HIO algorithm. The value $\beta = 0.4$ was used. A) The number of HIO iterations, n_{HIO}, are changed while the number of GS iterations, $n_{GS} = 1$, is kept constant. B) n_{GS} is changed while the cycle length $n_{HIO} + n_{GS} = 100$ is kept constant.

tion can be found by changing all three parameters simultaneously. The best combination of β, n_{HIO} and n_{GS} is then found by studying the minimum of sum of the mean and standard deviation from 100 reconstructions, each with 1000 iterations. The combination that yields the smallest mean and standard deviation will then give the most optimal combination. For a parabolic dip with $w = 0.01$ µm and $L = 500$ µm the best combination was found to be $\beta = 0.3$, $n_{HIO} = 170$ and $n_{GS} = 20$. The optimal combination for a sinusoidal curve and a Gaussian function could be found in a similar way. However, as the calculations were rather costly numerically, this was not prioritized within this thesis.

In the previous section we noticed that a reconstruction with error of the order 10^{-4} was qualitatively similar to the known height profile and the other reconstructions. It was therefore considered to have reached qualitative convergence. Due to the sheer number of reconstructions studied in Figures 5.12 and 5.13 we have not been able to study their qualitative behaviour directly. However, it is reasonable to believe that most of the reconstructions reached qualitative convergence as most of the sum of the mean and standard deviations were below the threshold value of 10^{-4}.

5.6 Reconstructing the surface morphology in GISAXS geometry

In the previous two sections reconstruction algorithms were explored using simulated height profiles. Lastly in this thesis, the reconstruction algorithms will be applied to the form factor of an island in the GISAXS geometry as derived in section 2.5. The differential cross section in the GISAXS geometry was in section 5.3 explored using an island of hemi-spherical shape. As argued in section 2.5 the intensity is proportional to the dif-

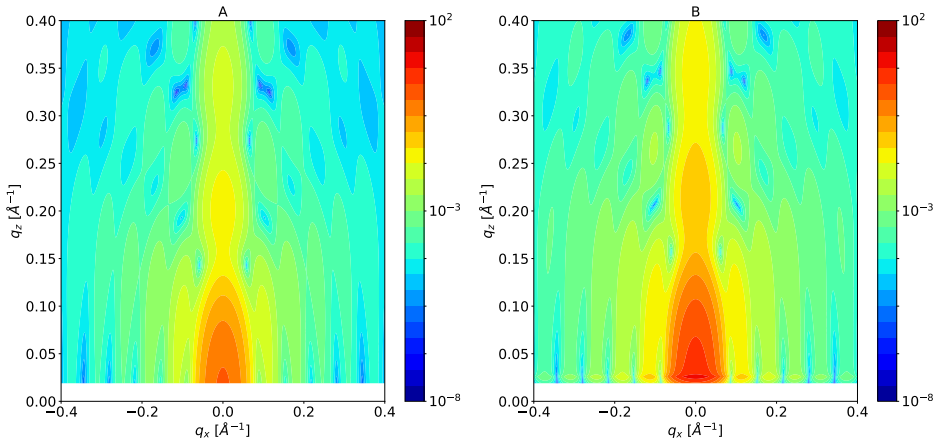

Figure 5.14: The form factor $|\mathscr{F}|^2$ of an island of hemi-spherical shape with $R = W = H = 50$ Å. A) Born approximation (BA). B) Distorted wave Born approximation (DWBA) with Yoneda peak at q_z corresponding to critical angle.

ferential cross section, which is itself proportional to the absolute square of the total form factor. The form factor can therefore be used as an input for the reconstruction algorithms.

First, the form factor of a hemi-sphere in the GISAXS geometry and the intensity of a parabolic height profile are compared. Figure 5.14A and 5.14B show the form factor of the hemi-sphere in the GISAXS geometry using the BA and the DWBA. The Yoneda peak is visible only in Figure 5.14B as it is a result of differences in the reflection amplitudes, as mentioned in section 5.3. Figure 5.15B shows the intensity of the parabolic height profile in Figure 5.15A. Note that the colorbar values are slightly different to Figures 5.14A and 5.14B to increase the visibility. At small values of q_z, the intensity from the BA is somewhat similar to the intensity of the parabolic height profile. Otherwise, the intensities are quite different.

Since the intensities are quite different, we expect the reconstructions to go badly. In hope for best result the form factor from the BA is used for reconstruction as it is the most similar to the intensity for a parabolic shape. Figure 5.16 show reconstructions for different L and q_z. In addition, different reconstruction algorithms with different parameters has been used. In all reconstructions the maximum number of iterations were set to 10^4. The reconstruction error for all reconstructions in Figure 5.16 were oscillating badly around 1. Surprisingly, reconstructions 2 and 4 in Figures 5.16A-C and reconstruction 4 in Figure 5.16D have shapes similar to a parabolic dip. However, the heights and widths are not as expected.

The phase reconstruction method and the DWBA and the BA are models describing a rather complex problem. The former assumes a homogeneous surface morphology with index of refraction n_S as illustrated in Figure 5.17B. In the derivation of the DWBA and BA form factor, outlined in section 2.5, an island is placed on a substrate with corresponding indexes of refraction n_I and n_S. This is visualized in Figure 5.17A. Additionally, the form factor, equation 2.29, only takes into account n_I and its deviation from the index of

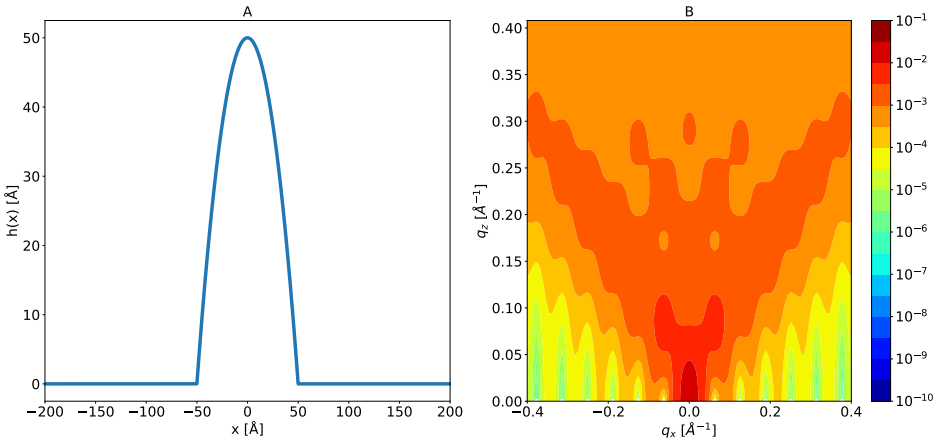

Figure 5.15: A) Parabolic height profile. B) The corresponding intensity to the height profile in A.

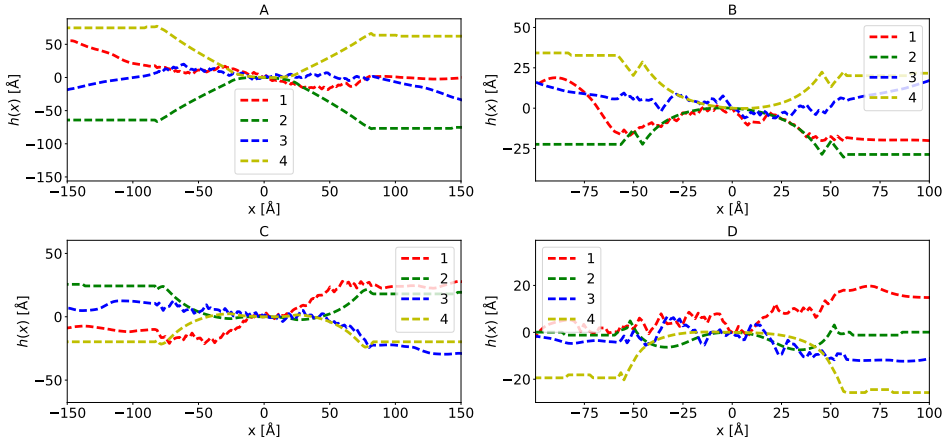

Figure 5.16: Reconstructions from the form factor of a hemi-spherical island of $R = W = H = 50$ Å using only the Born approximation. A) $L = 150$ Å, $q_z = 0.03$ Å^{-1}. B) $L = 100$ Å, $q_z = 0.03$ Å^{-1}. C) $L = 150$ Å, $q_z = 0.12$ Å^{-1}. D) $L = 100$ Å, $q_z = 0.12$ Å^{-1}. All reconstructions are done with 10^4 iterations using the following algorithms: 1) HIO ($\beta = 0.5$), 2) GS, 3) GS/HIO ($\beta = 0.3$, $n_{GS} = 20$, $n_{HIO} = 170$), 4) GS/HIO ($\beta = 0.5$, $n_{GS} = 5$, $n_{HIO} = 95$) followed by 200 iterations with GS.

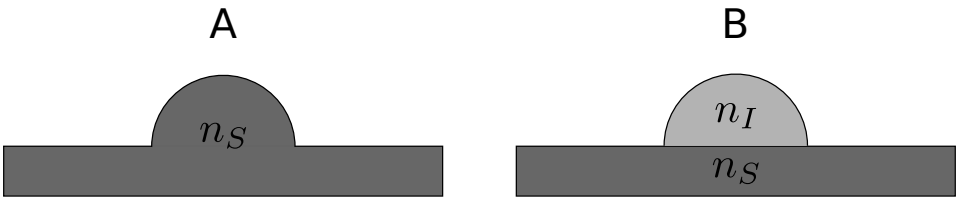

Figure 5.17: A) Homogeneous substrate with a parabolic peak having index of refraction n_S. B) Hemi-spherical island on substrate with indexes of refraction n_I and n_S, respectively.

refraction of vacuum, unity. n_S is embedded into the reflection amplitudes $r_{0,1}^{in}$ and $r_{0,1}^{sc}$. However, the contrast between n_S and n_I is also believed to be an important term in the form factor.

Chapter 6

Conclusion and outlooks

In X-ray imaging inversion of the scattering data is a comprehensive problem and amounts to the problem of phase determination. Without the phase information a direct inversion of the scattering data to reconstruct the scattering object is impossible. Possible phase reconstruction techniques involve fitting experimental parameters to a model and the use of iterative algorithms in coherent X-ray imaging. The former is built on the assumption that the incoming beam is a plane wave and is in need of a correction of the beam divergence. The latter utilizes oversampling in Fourier space to reconstruct the lost phase information. A possible improvement to the data models is to discard the plane wave assumption in favour of an experimentally more realistic beam, the Gaussian beam. The Gaussian beam is described by its beam waist and corresponding divergence angle, needing no correction for the beam divergence.

This thesis has investigated the reflection of the Gaussian beam using the angular decomposition method. The intensity and phase of a propagating Gaussian beam was found to be in good agreement with the mathematical expression derived from the Helmholtz equation. When studying the reflection on a flat surface the angular decomposition method enables us to study the reflection of each plane wave component using the Fresnel reflection amplitudes. The resulting reflected Gaussian beam is then a sum over the reflected plane wave components. Extending to the study of reflecting surfaces of higher complexity it was proposed that the reflection amplitudes could similarly be used when investigating the reflected Gaussian beam. This thesis was limited to multilayered surfaces and islands on substrates in the grazing incidence small-angle geometry. We have shown that in the limit of huge beam waists the reflectivity in both cases are very similar to that of a plane wave. Further work should investigate how to determine if this method works for a Gaussian beam with an arbitrary beam waist. Gaussian beams with narrow beam waist were found to lack important reflectivity details, suggesting that these Gaussian beams are not suitable in reflectivity experiments.

Coherent X-ray imaging enables the phase information to be found given that the diffraction pattern is oversampled. This thesis was limited to the study of surface morphology of a rough surface in grazing incidence. In grazing incidence the footprint is

elongated and will be approximately one dimensional. Applying an iterative algorithm to the oversampled diffraction pattern will reconstruct the phase information and the surface morphology can be found. The Gerchberg-Saxton algorithm was studied and used to reconstruct different surface morphologies, but was found to stagnate quickly. The Hybrid input-output algorithm was found to perform slightly better than the Gerchberg-Saxton algorithm. However, as with the Gerchberg-Saxton, the algorithm stagnated early. Ref. [21] has observed that the reconstruction morphology improves rapidly using the Hybrid input-output algorithm even though the error decreases little. By subsequently applying a few iterations of the Gerchberg-Saxton algorithm, we have shown that the error decreases rapidly. The combination algorithm was applied to a surface morphology of an island on a substrate. Some of the reconstructions successfully retrieved the qualitative shape of the hemisphere. However, the height and width of the hemispherical shape did not correspond well with the size of the island.

Each reconstruction was initialized with random phases resulting in different solutions with different reconstruction errors. Ref. [24] argued that constant initial phases gave better result for the Gerchberg-Saxton algorithm in the case of centrosymmetric intensity and density. Different initialization of the phases was not investigated during this thesis, but could be a possible continuation of this work.

An ambiguity that appears when doing reconstructions are the presence of a dual solution. Contrary to the discussion in Ref. [36], we were not able to verify the proper solution using intensity measurements at different incident angles. Additionally, according to Ref. [17] it is enough to oversample the diffraction pattern in two and three dimensions in order to obtain a unique solution. Future work should therefore expand our study to investigate two-dimensional surface morphology.

Bibliography

[1] E. Karud, *Study of the reflection of Gaussian beams in the X-ray regime*. Project work at NTNU, 2018.

[2] J. Als-Nielsen and D. McMorrow, *Elements of modern X-ray physics*. Chichester: Wiley, 2nd ed., 2011.

[3] S. T. Chourou, A. Sarje, X. S. Li, E. R. Chan, and A. Hexemer, "HipGISAXS : A High Performance Computing Code for Simulating Grazing Incidence X-Ray Scattering Data Supporting Information," *Journal of Applied Crystallography*, vol. 46, no. 6, pp. 1781–1795, 2013.

[4] D. Y. C. Durniak, M. Ganeva, G. Pospelov, W. Van Herck, J. Wuttke, "Software for simulating and fitting X-ray and neutron small-angle scattering at grazing incidence," 2018.

[5] J. R. Levine, J. B. Cohen, Y. W. Chung, and P. Georgopoulos, "Grazing-incidence small-angle X-ray scattering: new tool for studying thin film growth," *Journal of Applied Crystallography*, vol. 22, no. 6, pp. 528–532, 1989.

[6] A. Naudon and D. Thiaudiere, "Grazing-Incidence Small-Angle Scattering. Morphology of Deposited Clusters and Nanostructure of Thin Films," *Journal of Applied Crystallography*, vol. 30, no. 5, pp. 822–827, 1997.

[7] O. Glatter and O. Kratky, *Small angle X-ray scattering*. London: Academic Press, 1982.

[8] J. Daillant and A. Gibaud, eds., *X-ray and Neutron Reflectivity*, vol. 770 of *Lecture Notes in Physics*. Berlin, Heidelberg: Springer Berlin Heidelberg, 2009.

[9] M. Rauscher, R. Paniago, H. Metzger, Z. Kovats, J. Domke, J. Peisl, D. Pfannes, J. Schulze, and I. Eisele, "Grazing incidence small angle x-ray scattering from free-standing nanostructures," *Journal of Applied Physcs*, vol. 86, no. 12, 1999.

[10] L. G. Parratt, "Surface Studies of Solids by Total Reflection of X-rays," *Physical Review*, vol. 95, no. 2, 1954.

[11] V. Holý, J. Kubêna, I. Ohlídal, K. Lischaka, and W. Plotz, "X-ray reflection from rough layered systems," *Physical Review B*, vol. 47, no. 23, pp. 896–903, 1993.

[12] S. Gibaud and S. Hazra, "X-ray reflectivity and diffuse scattering," *Current Science*, vol. 78, no. 12, 2000.

[13] G. Renaud, R. Lazzari, and F. Leroy, "Probing surface and interface morphology with Grazing Incidence Small Angle X-Ray Scattering," *Surface Science Reports*, vol. 64, no. 8, pp. 255–380, 2009.

[14] A. Gibaud, G. Vignaud, and S. K. Sinha, "The correction of geometrical factors in the analysis of X-ray reflectivity," *Acta Crystallographica Section A*, vol. 49, no. 4, pp. 642–648, 1993.

[15] M. Mcguirk and C. K. Carniglia, "An angular spectrum representation approach to the Goos-Hanchen shift," *J. Opt. Soc. Am.*, vol. 67, no. 1, pp. 103–107, 1977.

[16] H. Yu, X. Jiang, J. Yang, W. Qi, and M. Wang, "Analytical model for the grazing reflection of a narrow beam," *Optics Letters*, vol. 31, no. 18, pp. 2747–2749, 2006.

[17] J. Miao, R. L. Sandberg, and C. Song, "Coherent X-Ray Diffraction Imaging," *IEEE Journal of Selected Topics in Quantum Electronics*, vol. 18, no. 1, pp. 399–410, 2012.

[18] J. Miao, P. Charalambous, J. Kirz, and D. Sayre, "Extending the methodology of X-ray crystallography to allow imaging of micrometre-sized non-crystalline specimens," *Letters to Nature*, vol. 400, pp. 342–344, 1999.

[19] Y. Takahashi, Y. Noshino, R. Tsutsumi, N. Zettsu, E. Matsurbara, K. Ymamauchi, and T. Ishikawa, "High-resolution projection image reconstruction of thick objects by hard x-ray diffraction microscopy," *Physical Review B*, vol. 82, pp. 1–5, 2010.

[20] J. R. Fienup, "Reconstruction of an object from the modulus of its Fourier transform," *Optics Letters*, vol. 3, no. 1, pp. 27–29, 1978.

[21] J. R. Fienup, "Phase retrieval algorithms : a comparison," *Applied Optics*, vol. 21, no. 15, 1982.

[22] J. Miao, D. Sayre, and H. N. Chapman, "Phase retrieval from the magnitude of the Fourier transforms of nonperiodic objects," *J. Opt. Soc. Am. A*, vol. 15, no. 6, pp. 1662–1669, 1998.

[23] B. R. W. Gerchberg and W. O. Saxton, "A Practical Algorithm for the Determination of Phase from Image and Diffraction Plane Pictures," *Optik*, vol. 35, no. 2, 1972.

[24] T. Thimons and L. Wittle, "Investigating the Gerchberg-Saxton Phase Retrieval Algorithm," pp. 189–199, 2018.

[25] D. J. R. C. Griffiths, *Introduction to electrodymanics*. Upper Saddle River, N.J: Prentice Hall, 3rd ed., 1999.

[26] P. M. Morse and H. Feshbach, *Methods of theoretical physics : Pt. 2 : Chapters 9 to 13*. New York: McGraw-Hill, 1953.

[27] B. E. A. Saleh and M. C. Teich, *Fundamentals of Photonics*. United States: Interscience, 2nd ed., 2013.

[28] M. Milosevic, "Fresnel Equations," in *Internal Reflection and ATR Spectroscopy*, pp. 39–54, Hoboken, NJ, USA: John Wiley & Sons, Inc., apr 2012.

[29] E. Hecht, *Optics: Pearson New International Edition*. Pearson Education Limited, 2013.

[30] M. Tolan, *X-ray scattering from soft-matter thin films : materials science and basic research*. Berlin: Springer, 1999.

[31] B. D. Cullity and S. R. Stock, *Elements of X-ray diffraction*. Prentice Hall, 3rd ed., 2001.

[32] I. Michio and K. Feiyu, "Small-Angle X-ray Scattering," in *Materials Science and Engineering of Carbon - Characterization, pp.1-1*, Elsevier, 2016.

[33] R. P. Riesz and R. Simon, "Reflection of a Gaussian beam from a dielectric slab," *J. Opt. Soc. Am. A*, vol. 2, no. 11, pp. 1809–1817, 1985.

[34] S. Kozaki and H. Sakurai, "Characteristics of a Gaussian beam at a dielectric interface," *J. Opt. Soc. Am.*, vol. 68, no. 4, pp. 508–514, 1978.

[35] H. Yu, X. Jiang, J. Yang, W. Qi, and M. Wang, "Generalized reflection and transmission of beams," *Physical Review A*, vol. 78, no. 3, p. 033827, 2008.

[36] I. A. Vartanyants, J. A. Pitney, J. L. Libbert, and I. K. Robinson, "Reconstruction of surface morphology from coherent x-ray reflectivity," *Physical Review B*, vol. 55, no. 19, pp. 193–202, 1997.

[37] M. Sutton, S. G. J. Mochriet, T. Greytak, S. E. Nagler, L. E. Berman, G. A. Held, and G. B. Stephenson, "Observation of speckle by diffraction with coherent X -rays," *Letters to Nature*, vol. 352, no. August, pp. 608–610, 1991.

[38] J. Miao and D. Sayre, "On possible extensions of X-ray crystallography through diffraction-pattern oversampling research papers," *Acta Crystallographica Section A: Foundations of Crystallography*, pp. 596–605, 2000.

[39] J. R. Fienup, "Reconstruction of a complex-valued object from the modulus of its Fourier transform using a support constraint," *J. Opt. Soc. Am. A*, vol. 4, no. 1, pp. 118–123, 1987.

[40] J. L. Libbert, R. Pindak, S. B. Dierker, and I. K. Robinson, "Speckle in coherent x-ray reflectivity from Si(111) wafers," *Physical Review B*, vol. 56, no. 11, pp. 6454–6457, 1997.

[41] W. O. Saxton, *Computer techniques for image processing in electron microscopy*. New York: Academic Press, 1978.

[42] J. R. Fienup, C. C. Wackerman, and A. Arbor, "Phase-retrieval stagnation problems and solutions," *J. Opt. Soc. Am. A*, vol. 3, no. 11, pp. 1897–1907, 1986.

[43] J. R. Fienup, "Iterative method applied to image reconstruction and to computer-generated holograms," *Optical engineering*, vol. 19, no. 3, 1980.

[44] C. Guo, S. Liu, and J. T. Sheridan, "Iterative phase retrieval algorithms . I: optimization," *Applied optics*, vol. 54, no. 15, pp. 4698–4708, 2015.

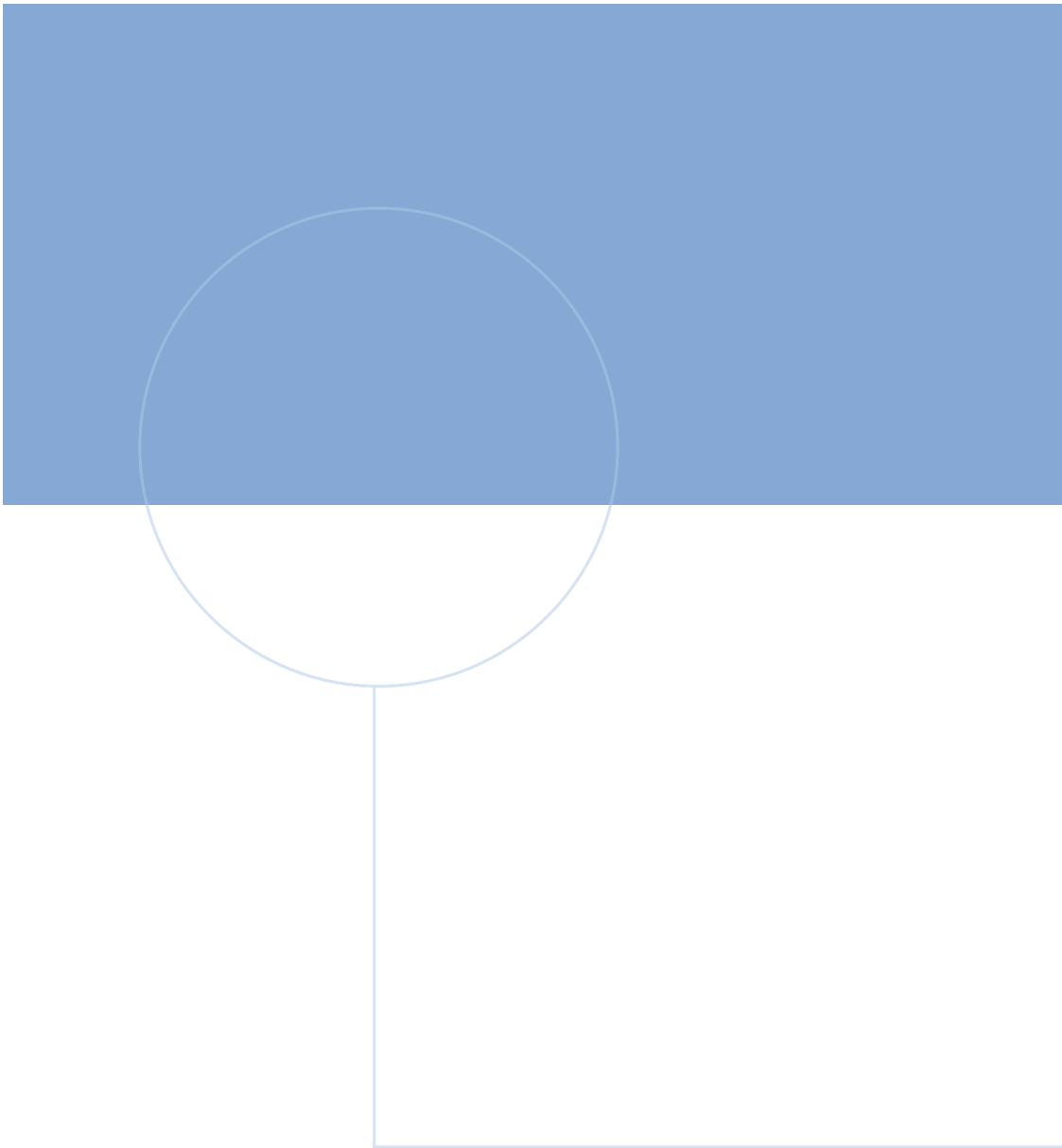

NTNU

Kunnskap for en bedre verden